

# Effect of element doping and substitution on the electronic structure and macroscopic magnetic properties of SmFe<sub>12</sub>-based compounds

Takuya Yoshioka


*Department of Applied Physics, Tohoku University, Sendai, Miyagi 980-8579, Japan;*  
*ESICMM, National Institute for Materials Science, Tsukuba, Ibaraki 305-0047, Japan;*  
*Center for Spintronics Research Network, Tohoku University, Sendai, Miyagi 980-8577, Japan;*  
*and Strategic Technology Center, TIS Inc., Koto, Tokyo 135-0061, Japan*

Hiroki Tsuchiura

*Department of Applied Physics, Tohoku University, Sendai, Miyagi 980-8579, Japan;*  
*ESICMM, National Institute for Materials Science, Tsukuba, Ibaraki 305-0047, Japan;*  
*and Center for Spintronics Research Network, Tohoku University, Sendai, Miyagi 980-8577, Japan*

Pavel Novák 

*Institute of Physics of ASCR, Cukrovarnická, Prague 6 162 00, Czech Republic*

 (Received 1 August 2021; revised 18 November 2021; accepted 21 December 2021; published 3 January 2022)

The mechanisms underlying the enhancement of magnetic anisotropies (MAs) of Sm ions, owing to valence electrons at the Sm site and the screened nuclear charges of ligands, are clarified using a detailed analysis of crystal fields (CF). In order to investigate the finite-temperature magnetic properties, we developed an effective spin model for SmFe<sub>12</sub>X (X=H, B, C, and N) and SmFe<sub>11</sub>M (M=Ti, V, and Co), where the magnetic moments, CF parameters, and exchange fields were determined by first-principle calculations. Using this model, the MA constants and magnetization curves at finite temperatures were investigated using a recently introduced analytical method [Yoshioka, Tsuchiura, and Novák, *Phys. Rev. B* **102**, 184410 (2020)]. In SmFe<sub>12</sub>X, the doped light elements X are assumed to be at the 2*b* site, and in SmFe<sub>11</sub>M, the substitution site of Fe is systematically investigated for all inequivalent 8*f*, 8*i*, and 8*j* sites. We found that the first-order MA constant  $K_1$  is increased by a factor of about two when hydrogen is doped to the 2*b* site and when Fe is replaced by Ti or V at the 8*j* site, owing to the attraction of the prolate 4*f* electron cloud to the screened positive charges of the surrounding ligand ions. We found that when Fe is replaced by Co, the MA increases at all temperatures regardless of the substitution site. The substituted Co attracts electrons, which reduces the electron density in the region from the Sm site to the empty 2*b* site. This causes the 4*f* electron cloud at the Sm site to be fixed along the *c*-axis direction, which improves the MA. The calculated temperature dependence of  $K_1(T)$  and  $K_2(T)$  in SmFe<sub>11</sub>Co qualitatively reproduces the experimental results in the case of Sm(Co<sub>*x*</sub>Fe<sub>1-*x*</sub>)<sub>12</sub> for  $x = 0.1$  and 0.07. The first-order magnetization process is observed at low temperatures in SmFe<sub>12</sub> itself and in many variations of SmFe<sub>12</sub>-based compounds prepared using element doping and substitution. This is mainly due to the competition between the conditions  $K_1 > 0$  and  $K_2 < 0$ , and that of  $K_1 < -6K_2$  owing to the ThMn<sub>12</sub> structure having a vacancy at the 2*b* site.

DOI: [10.1103/PhysRevB.105.014402](https://doi.org/10.1103/PhysRevB.105.014402)

## I. INTRODUCTION

Intensive research has been conducted on developing new rare-earth (*R*) lean permanent magnetic materials, which have strong magnetic properties comparable to those of Nd-Fe-B. Hence, magnetic materials possessing a ThMn<sub>12</sub> structure, which have a high proportion of Fe relative to *R*, are again attracting research attention [1–5]. However, the substitution of stabilizing elements is especially important [6–18]. For example, nitrogenation of NdFe<sub>12</sub> compounds improves the magnetic properties considerably [1,2,18]. Thus, elemental doping and substitution of the ThMn<sub>12</sub> series of compounds are being intensively researched for practical applications, and

understanding the basic principles governing their behavior is required, based on the electronic theory.

Recently, a thin film of SmFe<sub>12</sub> was synthesized and its intrinsic magnetic properties were investigated experimentally [9]. The magnetic properties of SmFe<sub>12</sub> can be improved by substituting Co for Fe [9,11,13] and the addition of B increases its coercivity, which has attracted much attention in terms of its applicability [14].

On the other hand, theoretical studies have long been conducted [18–24]. Using a simple model, Kuz'min *et al.* [19] found that the leading term of the CF parameter  $A_2^0$  is negative for Fe-based RFe<sub>12-*x*</sub>M<sub>*x*</sub> compounds regardless of the type of *R*. Harashima *et al.* [18,20] and Körner *et al.* [21]

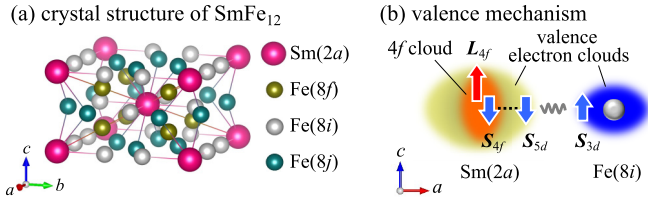


FIG. 1. (a) Crystal structure of  $\text{SmFe}_{12}$  and (b) illustration of the valence mechanism [24,25].

investigated the effect of nitridation on the magnetic properties of a series of 1-12. For  $\text{SmFe}_{12}$ , it was found that nitridation changes the sign of  $A_2^0$  from negative to positive. Ke *et al.* [22] have extensively investigated the effects of doping and substitution systematically for  $R\text{Fe}_{12}$ -based compounds for  $R=Y$  and Ce. Their study revealed that the Fe dominated transition metal sublattice has uniaxial magnetic anisotropy in the range of the investigated compounds, which are  $\text{YFe}_{12}$  and  $\text{YFe}_{11}\text{TiX}$  ( $X=H, C, N$ ). The above analyses are based on the simple model or first-principles calculations at absolute zero. Delange *et al.* [23] studied the effect of N and Li doping on the finite temperature MA of  $\text{SmFe}_{12}$  in detail. However, the effect of substitution, which is important in the 1-12 system, was not taken into account and magnetization curves that can be compared to experiments were not presented. We calculated the MA constants at finite temperatures as well as the magnetization curves for the 1-12 system [24]. However, we did not discuss the effect of doping and substitution on the  $\text{SmFe}_{12}$ . Therefore, detailed analysis of the finite-temperature magnetic properties must be performed, including magnetic anisotropy constants and magnetization curves of  $\text{SmFe}_{12}$  compounds with doping and substitution. In this study, we analyze the electronic states of  $\text{SmFe}_{12}$ -based compounds by considering elemental doping and substitution independently. In addition, we construct an effective spin model based on these electronic states and analyze their macroscopic magnetic properties at finite temperatures. Figure 1 shows (a) the crystal structure and (b) the mechanism underlying MA.

In our previous paper [24], we reported that the uniaxial MA in  $\text{SmFe}_{12}$  is a consequence of the Coulombic interaction between the valence and  $4f$  electron clouds. However, a quantitative and comprehensive understanding, based on the electronic structure that has undergone doping and substitution, of the mechanism underlying the MA is still insufficient, which is essential for the efficient application of  $\text{SmFe}_{12}$ -based compounds.

The purpose of this study was to extract the macroscopic magnetic properties of  $\text{SmFe}_{12}$ -based compounds at finite temperatures based on electronic theory using a recently developed reliable method [24–28]. In this study, we focus on the  $\text{SmFe}_{12}X$  ( $X=H, B, C, \text{ and } N$ ) and  $\text{SmFe}_{11}M$  ( $M=\text{Ti, V, and Co}$ ) compounds. The electron structure and finite-temperature magnetic properties are investigated within the linear theory for CF Hamiltonian [24].

This paper is organized as follows. In Sec. II, we introduce the effective spin model and analytical method for  $\text{SmFe}_{12}$ -based compounds. In Sec. III, we briefly outline the mechanism underlying the MA on  $R$  ion in  $R$ -transition-metal compounds. In Sec. VI, we present the doping and substitution

effects on the electronic structure and MA. The macroscopic MA constants at finite temperatures and magnetization curves, along with a brief summary are detailed in Sec. V.

## II. MODEL AND METHOD

In this study, we investigate the macroscopic magnetic properties from the electronic structure of the  $\text{SmFe}_{12}X$  ( $X=H, B, C, \text{ and } N$ ) and  $\text{SmFe}_{11}M$  ( $M=\text{Ti, V, and Co}$ ) shown in Fig. 2. For this purpose, we determine the model parameters using first-principle calculations and construct an effective spin model. In this section, we describe the model Hamiltonian and the method to determine its parameters. Next, we utilize the method to investigate the magnetic properties at finite temperatures.

### A. Model Hamiltonian for $R$ -transition-metal compounds

In order to investigate the bulk magnetic properties, we assume homogeneity of the partial magnetization  $M^{\text{TM}}$  and partial anisotropy constant  $K_1^{\text{TM}}$ , excluding the contribution of the  $4f$  electrons. The parameters  $M^{\text{TM}}$  and  $K_1^{\text{TM}}$  are mainly associated with the transition-metal elements. To consider the effect of a small amount of elemental doping and substitution with respect to  $\text{SmFe}_{12}$ , we assume a similar uniaxial MA of  $\text{SmFe}_{11}\text{Ti}$ , which has been confirmed experimentally [7,29]. In this case, the Hamiltonian of the system can be written in terms of the following two-sublattice model [24,26,30,31]:

$$\hat{\mathcal{H}} = \sum_{j=1}^{n_R} \hat{\mathcal{H}}_{R,j} + V K_1^{\text{TM}}(T) [1 - (M^{\text{TM}} \cdot \mathbf{n}_c)^2] - V M^{\text{TM}}(T) \cdot \mathbf{B}, \quad (1)$$

where  $\hat{\mathcal{H}}_{R,j}$  is a Hamiltonian for single  $R$  ion at the site  $j$ ,  $M^{\text{TM}}(T)$  is the partial magnetization excluding the contribution of the  $R$  ions,  $\mathbf{n}_c$  is the unit vector along the  $c$  axis, and  $n_R$  is the number of  $R$  ions in the volume of the cell  $V$  to be considered. Hereafter  $j$  is omitted for simplicity. The  $\hat{\mathcal{H}}_R$  can be written as [24,32,33]:

$$\hat{\mathcal{H}}_R = \hat{\mathcal{H}}_{\text{so}} + \hat{\mathcal{H}}_{\text{ex}} + \hat{\mathcal{H}}_{\text{CF}} + \hat{\mathcal{H}}_{\text{Z}}, \quad (2)$$

$$\hat{\mathcal{H}}_{\text{so}} = \xi \sum_{i=1}^{n_{4f}} \hat{\mathbf{l}}_i \cdot \hat{\mathbf{s}}_i, \quad (3)$$

$$\hat{\mathcal{H}}_{\text{ex}} = 2\mu_B \mathbf{B}_{\text{ex}}(T) \cdot \sum_{i=1}^{n_{4f}} \hat{\mathbf{s}}_i, \quad (4)$$

$$\hat{\mathcal{H}}_{\text{CF}} = \sum_{l,m} \frac{A_l^m \langle r^l \rangle}{a_{l,m}} \sum_{i=1}^{n_{4f}} t_i^m(\hat{\theta}_i, \hat{\phi}_i), \quad (5)$$

$$\hat{\mathcal{H}}_{\text{Z}} = \mu_B \mathbf{B} \cdot \sum_{i=1}^{n_{4f}} (\hat{\mathbf{l}}_i + 2\hat{\mathbf{s}}_i), \quad (6)$$

where the summation of  $\sum_{i=1}^{n_{4f}}$  is taken over  $4f$  electrons in the  $R$  ion.  $\hat{\mathcal{H}}_{\text{so}}$  is the spin-orbit interaction between the spin ( $\hat{\mathbf{s}}_i$ ) and orbital ( $\hat{\mathbf{l}}_i$ ) angular momenta, with a coupling constant  $\xi$ .  $\hat{\mathcal{H}}_{\text{ex}}$  is the exchange interaction between the spin moment and temperature-dependent exchange field  $\mathbf{B}_{\text{ex}}(T)$ , where  $\mu_B$  is the Bohr magneton.  $\hat{\mathcal{H}}_{\text{CF}}$  is the CF Hamiltonian, where  $A_l^m \langle r^l \rangle$

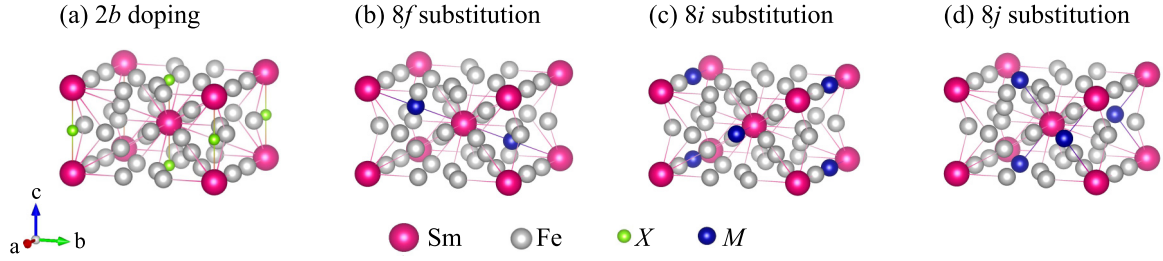


FIG. 2. Crystal structures of (a)  $\text{SmFe}_{12}X$  ( $X=\text{H, B, C, and N}$ ) for  $2b$ -site doping and  $\text{SmFe}_{11}M$  ( $M=\text{Ti, V, and Co}$ ) with substitution for each Fe (b)  $8f$ , (c)  $8i$ , and (d)  $8j$  sites in  $\text{SmFe}_{12}$ .

is the CF parameter for the  $j$ th  $R$  site,  $a_{l,m}$  is a numerical factor [34,35],  $t_l^m(\hat{\theta}_i, \hat{\phi}_i)$  is the tesseral harmonic function of the polar and azimuthal angle  $\hat{\theta}_i$  and  $\hat{\phi}_i$ .  $\hat{H}_Z$  is the Zeeman term with an applied field  $\mathbf{B}$ .

The hierarchy of the energy scale of each term is as follows:

$$\hat{H}_{\text{so}} \gg \hat{H}_{\text{ex}} \gg \hat{H}_{\text{CF}} \sim \hat{H}_Z. \quad (7)$$

In this situation, it is possible to map the density functional theory (DFT) to the CF theory within the first order of the CF term [36]. Therefore, we apply our linear theory for the CF [24] to the two-sublattice model to clarify the finite temperature magnetic properties, where we apply the  $LS$  coupling scheme with the assumption of a trivalent  $R$ . In the treatment of  $\hat{H}_{\text{so}}$ , we should note that because the  $LS$  coupling in Sm compounds is weak compared with those of the other  $R$ , the excited  $J$  multiplets must be included [24,32,33,37–39]. Details are shown in Appendix A.

For  $\text{SmFe}_{12}X$  ( $X=\text{H, B, C, and N}$ ), the doped light elements are assumed to be at the  $2b$  site [Fig. 2(a)]. In this case, the lattice constants as for  $\text{SmFe}_{12}$  [9] that is,  $a = b = 8.35 \text{ \AA}$  and  $c = 4.8 \text{ \AA}$  are used. The substituted compounds of  $\text{SmFe}_{11}M$  ( $M=\text{Ti, V, and Co}$ ) are systematically investigated for all possible replacement sites  $8f$ ,  $8i$ , and  $8j$  for each  $M$ . The experimentally determined lattice constants are used for the first-principle calculations, where  $a = b = 8.54 \text{ \AA}$  and  $c = 4.78 \text{ \AA}$  [7],  $a = b = 8.5205 \text{ \AA}$  and  $c = 4.7693 \text{ \AA}$  [10], and  $a = b = 8.4 \text{ \AA}$  and  $c = 4.8 \text{ \AA}$  [9], for  $M=\text{Ti, V, and Co}$ , respectively.

Local distortions due to doping and substitution are expected to affect the results. In this study, however, we focus on the effect of chemical changes on the MA; thus, we simplified the internal structure by fixing it to the  $\text{SmFe}_{12}$  as (0.25,0.25,0.25) for  $8f$ , (0.359,0.000,0.000) for  $8i$ , and (0.270,0.500,0.000) for  $8j$  sites [20]. For reference, the energies of the systems for  $\text{SmFe}_{11}M$  studied in this study are shown in Appendix B. The results are comparable to those of the previous theoretical study [40].

## B. Model parameters determined by first-principle calculations

In this study, the model parameters are determined using DFT calculations. We use the full-potential linearized augmented plane wave plus local orbitals (APW + lo) method implemented in the WIEN2K code [41]. The Kohn-Sham equations are solved within the spin polarized generalized-gradient approximation (SGGA). The  $4f$  electron states cannot be

correctly described by local or semilocal approximations to DFT. Therefore, we treat them as core states of an atom, which corresponds to the so-called open-core method [42–47].

The total energy of the system in the DFT, as a function of the total charge density  $\rho(\mathbf{r})$ , has the following form [36,48]:

$$E[\rho(\mathbf{r})] = T_s[\rho(\mathbf{r})] + E_{\text{en}}[\rho(\mathbf{r})] + E_{\text{H}}[\rho(\mathbf{r})] + E_{\text{XC}}[\rho(\mathbf{r})], \quad (8)$$

where the right-hand side represents a sum of the noninteracting kinetic, electron-nucleus, Hartree, exchange-correlation (XC) energies.  $\rho(\mathbf{r})$  is decomposed to  $\rho(\mathbf{r}) = \rho_{4f}(\mathbf{r}) + \rho_{\text{rest}}(\mathbf{r})$ , where  $\rho_{\text{rest}}(\mathbf{r})$  is the total electron density excluding the  $4f$  electrons.

The change in the CF energy within the atomic sphere radius  $r_{\text{AS}}^R$  with respect to the change in the orientation of the  $4f$  electron cloud  $\Delta\rho_{4f}$  can be written as [36,49]

$$\Delta E_{\text{CF}} = \int_{|\mathbf{r}| < r_{\text{AS}}^R} \{V_{\text{en}}(\mathbf{r}) + V_{\text{H}}[\rho_{\text{rest}}^0(\mathbf{r})]\} \Delta\rho_{4f}(\mathbf{r}) d^3r, \quad (9)$$

where  $V_{\text{en}}(\mathbf{r})$  and  $V_{\text{H}}[\rho_{\text{rest}}^0(\mathbf{r})]$  are the Coulomb potential of the nuclei and the Hartree potential, respectively, which can be written in the following form [49]:

$$V_{\text{en}}(\mathbf{r}) = \frac{\delta E_{\text{en}}[\rho(\mathbf{r})]}{\delta \rho(\mathbf{r})} = -\frac{e^2}{4\pi\epsilon_0} \sum_n \frac{Z_n}{|\mathbf{r} - \mathbf{R}_n|}, \quad (10)$$

$$V_{\text{H}}[\rho_{\text{rest}}^0(\mathbf{r})] = \left. \frac{\delta E_{\text{H}}[\rho(\mathbf{r})]}{\delta \rho(\mathbf{r})} \right|_{\rho=\rho_{\text{rest}}^0} = \frac{e^2}{4\pi\epsilon_0} \int \frac{\rho_{\text{rest}}^0(\mathbf{r}')}{|\mathbf{r} - \mathbf{r}'|} d^3r', \quad (11)$$

where  $Z_n$  is the nuclear charge on the  $n$ th site and  $\rho_{\text{rest}}^0(\mathbf{r})$  is the total charge excluding the  $4f$  electrons, which is fixed to the self-consistent charge density. Moreover, the change in the expectation value of the CF Hamiltonian can be written as:

$$\Delta \langle \hat{H}_{\text{CF}} \rangle_{4f} = \sum_{l,m} \frac{A_l^m \langle r^l \rangle}{a_{l,m}} \Delta \left\langle \sum_{i=1}^{n_{4f}} t_l^m(\hat{\theta}_i, \hat{\phi}_i) \right\rangle_{4f}. \quad (12)$$

By comparing Eqs. (9) and (12), the CF parameters can be obtained in the following form:

$$A_l^m \langle r^l \rangle = a_{l,m} \int_{|\mathbf{r}| < r_{\text{AS}}^R} d^3r |R_{4f}(r)|^2 t_l^m(\theta, \phi) \times \{V_{\text{en}}(\mathbf{r}) + V_{\text{H}}[\rho_{\text{rest}}^0(\mathbf{r})]\} \quad (13)$$

where  $R_{4f}(r)$  is the radial part of the  $4f$  wave function and  $r_{AS}^R$  denotes the radius of an atomic sphere. As shown in Eq. (13), the aspherical part of  $V_H[\rho_{\text{rest}}^0(\mathbf{r})]$  denotes the CF acting on the  $4f$  electrons. In the actual calculation, the opencore method is applied to treat the  $4f$  electrons as spherical core electrons. In this case,  $\rho_{\text{rest}}^0(\mathbf{r})$  in Eq. (13) can be replaced with the total charge density  $\rho^0(\mathbf{r})$ , obtained using self-consistent calculations.

The exchange field  $B_{\text{ex}}(T)$  at  $T = 0$  K acting on the  $4f$  spin moments in the two-sublattice model in Eq. (4) can be obtained by comparing the change in the total energy  $\Delta E$  in DFT calculations with one in the expectation value of the exchange term  $\hat{\mathcal{H}}_{\text{ex}}$ :

$$\Delta \langle \hat{\mathcal{H}}_{\text{ex}} \rangle_{4f} = 2\mu_B \mathbf{B}_{\text{ex}}(0) \cdot \Delta \left\langle \sum_{i=1}^{n_{4f,j}} \hat{\mathbf{s}}_i \right\rangle_{4f}, \quad (14)$$

where  $\mu_B$  is the Bohr magneton. Since, the opencore method allows us to control the number of occupied  $4f$  electrons for each spin, it is possible to estimate the increase in energy when the total spin is rotated by  $180^\circ$ , within Hund's first rule. If the increase of total energy due to the spin flip is denoted as  $\Delta E$ ,  $B_{\text{ex}}$  can be obtained from the following equation [50–52]:

$$B_{\text{ex}}(0) = \Delta E / 4\mu_B S, \quad (15)$$

where  $S$  is the total spin angular momentum of the  $4f$  electrons. The partial magnetization  $M^{\text{TM}}(T)$  at  $T = 0$  K in Eq. (1) is obtained in the framework of SGGA as:

$$VM^{\text{TM}}(0) = \int_V [\rho_{\text{rest},\uparrow}^0(\mathbf{r}) - \rho_{\text{rest},\downarrow}^0(\mathbf{r})] dr^3, \quad (16)$$

where  $\rho_{\text{rest},\sigma}^0$  is the self-consistent charge density for spin  $\sigma$  excluding the  $4f$  electrons.

The following are the technical parameters required for electronic structure calculations using WIEN2K code (version 16.1). The number of  $k$  points within the whole Brillouin zone was set to  $8 \times 8 \times 14$ . The momentum space integrations are performed using the linear tetrahedron method with Blöchl correction. For  $\text{SmFe}_{12}\text{H}$ , 1406 basis functions with  $\text{RKmax}=4.0$  were used, and for all the other compounds 6063 basis functions with  $\text{RKmax}=6.0$  were used. The radius for Sm ions is  $r_{AS}^{\text{Sm}} = 3.2a_0$ , for  $M=\text{Fe}$ , Ti, V, and Co ions is  $r_{AS}^M = 2.21a_0$ , and for  $X=\text{H}$ , N, B, and C ions is  $r_{AS}^X = 1.32a_0$ , where  $a_0$  is the Bohr radius.

In analyzing the MA, it is important to investigate the dependence of the CF parameters on the  $r_{AS}^{\text{Sm}}$  for the series of systems. However, due to the significant computational resources required for determining this dependence, the maximum possible radius for Sm within which the atomic radii do not overlap,  $r_{AS}^{\text{Sm}} = 3.2a_0$ , was adopted in this study.

### C. Phenomenological parameters

For temperature dependence of  $M^{\text{TM}}(T)$  and  $K_1^{\text{TM}}(T)$ , we apply the phenomenological Kuz'min formula [53] and extended power law [54] under the uniformity

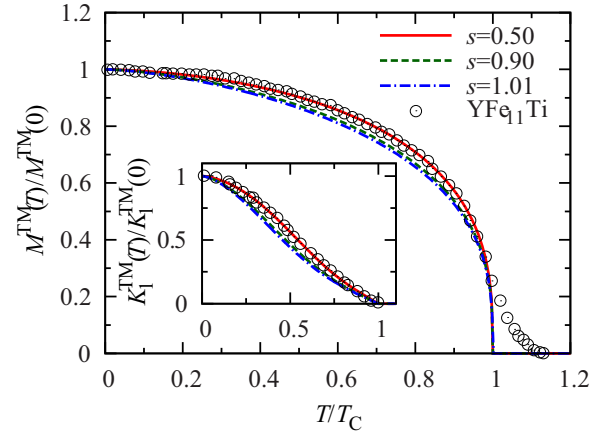


FIG. 3. TM-sublattice magnetization  $M^{\text{TM}}(T)$  and MA constant  $K_1^{\text{TM}}(T)$  (inset) for  $s = 0.50, 0.90$  [9], and  $1.01$  [9], used in the present calculations, where  $s$  is the shape parameter of the Kuz'min formula [53]. Open circles are experimental results of  $M^{\text{TM}}(T)$  and  $K_1^{\text{TM}}(T)$  in  $\text{YFe}_{11}\text{Ti}$  compounds [29], both of which are well fitted by  $s = 0.5$ ,  $C_1 = -0.263$ , and  $C_2 = -0.237$  in Eqs. (17) and (18).

assumption as:

$$\frac{M^{\text{TM}}(T)}{M^{\text{TM}}(0)} = \alpha(T), \quad (17)$$

$$\frac{K_1^{\text{TM}}(T)}{K_1^{\text{TM}}(0)} = \alpha^3(T) + \frac{8}{7}C_1[\alpha^3(T) - \alpha^{10}(T)] + \frac{8}{7}C_2 \left[ \alpha(T)^3 - \frac{18}{11}\alpha(T)^{10} + \frac{7}{11}\alpha(T)^{21} \right], \quad (18)$$

$$\alpha(T) = \left[ 1 - s \left( \frac{T}{T_C} \right)^{3/2} - (1-s) \left( \frac{T}{T_C} \right)^{5/2} \right]^{1/3}, \quad (19)$$

As shown above,  $M^{\text{TM}}(0)$  can be obtained from the first-principle calculations according to the Eq. (16), and for the MA constant  $K_1^{\text{TM}}(0)$ , we use the experimental value of  $\text{YFe}_{11}\text{Ti}$  at low temperatures as given in Ref. [29].  $T_C$  and  $s$  are the fitting parameters which are used to reproduce the experimental results of the temperature-dependent spontaneous magnetization.

For  $\text{SmFe}_{12}$ , the values of  $T_C = 555$  K and  $s = 1.01$  are used, which were determined by Hirayama *et al.* [9]. For  $\text{SmFe}_{12}X$  ( $X=\text{H}$ , B, C, and N), we use the dimensionless parameter  $T/T_C$  and  $s = 1.01$ , because experimental values of  $T_C$  do not exist. For  $\text{SmFe}_{11}M$  with an elemental substitution of  $M=\text{Ti}$ , V, and Co, we use  $T_C = 584$  [7], 634 [10], and 710 [9] K as the experimental value of Curie temperatures and  $s = 0.5, 0.5$ , and  $0.9$  [9] as the form factors in Eq. (19), respectively, where  $s = 0.5$  used for  $\text{SmFe}_{11}\text{Ti}$  and  $\text{SmFe}_{11}\text{V}$  is determined from  $\text{YFe}_{11}\text{Ti}$  as shown in Fig. 3. We note here that the experimental value of  $T_C$  and  $s$  for  $\text{SmFe}_{10.8}\text{Co}_{1.2}$  in Ref. Hirayama *et al.* [9] have been adopted as the model parameters for  $\text{SmFe}_{11}\text{Co}$ .

The MA constant  $K_1^{\text{TM}}(T)$  in Eq. (18) is expressed by the parameters  $s$ ,  $T_C$ ,  $K_1^{\text{TM}}(0)$ ,  $C_1$ , and  $C_2$ . Among these, the parameters  $s$  and  $T_C$  acquire material-specific values given in the previous paragraph. For remaining parameters  $K_1^{\text{TM}}(0)$ ,  $C_1$ , and  $C_2$ , we refer to the experimental data of  $\text{YFe}_{11}\text{Ti}$  [29].

From the fitting to  $\text{YFe}_{11}\text{Ti}$ , we determined  $C_1 = -0.263$ ,  $C_2 = -0.237$ , and  $VK_1^{\text{TM}}(0) = 47.7 \text{ K}/2f.u.$  The resulting temperature dependences of  $K_1^{\text{TM}}(T)$  are shown in Fig. 3. It should be noted that the  $K_1^{\text{TM}}(0)$  can be determined by first-principles calculations by introducing a spin-orbit interaction to the valence electrons, and the  $C_1$  and  $C_2$ , which are essentially material dependent parameters, should be obtained from the respective experimental results. However, it is difficult to have all of these parameters, so this will be a future issue.

#### D. Macroscopic magnetic properties

Similar to the method applied by Yoshioka *et al.*, [24] the first-order finite temperature perturbation theory is applied to the modified effective lowest- $J$  multiplet Hamiltonian, the approximate Gibbs free energy  $G(\mathbf{M}_s, T, \mathbf{B})$  (Eq. (61) as given in Ref. [24]) for the whole system can be obtained using the Legendre transformation for the Helmholtz free energy  $F(\mathbf{M}_s, T)$  (Eq. (62) in Ref. [24]) as follows:

$$G(\mathbf{M}_s, T, \mathbf{B}) = F(\mathbf{M}_s, T) - V\mathbf{M}_s(T) \cdot \mathbf{B}, \quad (20)$$

$$F(\mathbf{M}_s, T) = \sum_{j=1}^{n_R} \sum_{p=1}^3 \left[ k_{p,j}(T) + \sum_{q=1}^{\lfloor p/2 \rfloor} k_{p,j}^q(T) \cos(4q\Phi) \right] \times \sin^{2p} \Theta + VK_1^{\text{TM}}(T) \sin^2 \Theta + F(\mathbf{M}_s \mathbf{n}_c, T), \quad (21)$$

$\Theta$  and  $\Phi$  denote the polar and azimuthal angle of  $\mathbf{M}_s$ , respectively,  $\mathbf{n}_c$  is the unit vector along the  $c$  axis,  $\lfloor p/2 \rfloor$  indicates the greatest integer of  $p/2$ , and  $k_p^{(q)}(T)$  are the anisotropy constants of the  $4f$  shells for the  $j$ th  $R$  ion, part of which are given in Eqs. (56) and (57) in Ref. [24] and all necessary  $k_p^{(q)}$  with a fourfold rotational symmetry are mentioned in the Appendix C.  $\mathbf{M}_s(T)$  refers to the spontaneous magnetization for the whole system, which can be written as:

$$\mathbf{M}_s(T) = \left[ \frac{1}{V} \sum_{j=1}^{n_R} m_j(T) + M^{\text{TM}}(T) \right] \mathbf{n}_s, \quad (22)$$

where  $\mathbf{n}_s$  is the direction vector of  $\mathbf{M}_s$  and  $m_j(T)$  is the expectation value of the magnetic moment of the  $4f$  shell for the  $j$ th  $R$  ion, which are given in Eq. (46) in the Ref. [24].

The equilibrium condition of the system for a given  $T$  and  $\mathbf{B}$  is

$$G^{\text{eq}}(T, \mathbf{B}) = \min_{\mathbf{n}_s} G(\mathbf{M}_s, T, \mathbf{B}). \quad (23)$$

In practice, we determine the minimal  $G(\mathbf{M}_s, T, \mathbf{B})$  numerically by changing the direction of  $\mathbf{M}_s$ . Magnetization curves along the direction of an applied field are obtained using  $\partial G^{\text{eq}}(T, \mathbf{B})/\partial B$ .

### III. MECHANISM OF MA IN RARE-EARTH IONS

In this section, we first discuss the mechanism underlying MA induced by  $R$  ions in the  $R$ -transition-metal intermetallic compounds. Next, the relationship between the atomic configuration and MA in  $\text{SmFe}_{12}$  is reviewed.

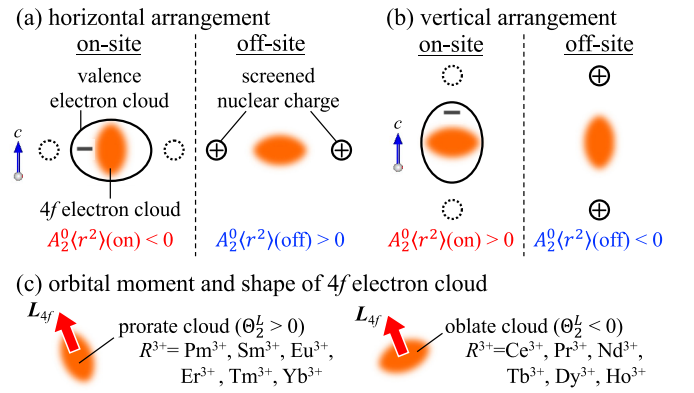


FIG. 4. Schematic of an on-site (left panel) and off-site (right panel) contribution to  $A_2^0(r^2)$  in (a) horizontal and (b) vertical arrangement of ligands, and (c) the orbital moment  $L_{4f}$  and the shape of the  $4f$  electron cloud, which are related by the equivalent factor  $\Theta_2^L$  in Eq. (A3). Ellipses with a minus sign and circles with a plus sign represent the valence electron clouds and screened nuclear charges, respectively.

#### A. General consideration

In  $R$  permanent magnet materials, the MA of  $R$  ions plays an important role. An MA is mainly determined by the CF acting on the  $4f$  electron cloud in the  $R$  ions. This CF at the  $R$  site is determined by the valence electron cloud surrounding the valence electrons and the screened nuclear charges of the ligand ions. The contribution of each of the  $4f$  electrons and screened nuclear charges to the electrostatic potential is sometimes called the valence and lattice contribution, respectively. However, it is difficult to clearly separate these contributions in intermetallic compounds. Here, we refer to each contribution as the on-site and off-site contribution, which is defined as the contribution from the charges inside and outside the atomic radius of the rare earths, respectively.

We show the effect of its on-site and off-site contributions on MA. Within our approximation, the MA constants can be written as a linear combination of the CF parameters, which can be decomposed into the on-site and off-site contributions. Here, we focus on  $A_2^0(r^2)$ , which is important for MA. The left and right panels in Figs. 4(a) and 4(b) schematically show the stable orientation of the  $4f$  electron cloud with respect to the CF created by the valence electron cloud and the screened positive charges, respectively. The direction of the orbital angular momentum with respect to the  $4f$  electron cloud is shown in (c).

Here, we consider a simple case where two ligands are arranged in the (a) horizontal and (b) vertical configuration as shown in the figure. When only the on-site contribution is considered, the valence electron cloud is oriented in the direction of the ligand, and the  $4f$  electron cloud is oriented away from it. In contrast, when only the off-site contribution is considered, the  $4f$  electron cloud is oriented in the direction of the screened nuclear charge. Because of the competition between the on-site and off-site contributions, the signs of the CF parameters  $A_2^0(r^2)(\text{on})$  and  $A_2^0(r^2)(\text{off})$  are opposite, as shown in the figure. The sign of  $A_2^0(r^2)$  is reversed depending on the ligand configuration (a) and (b).

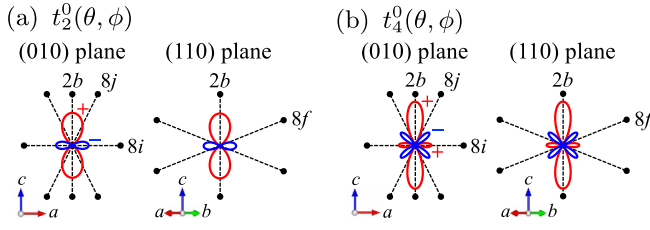


FIG. 5. Tesseral harmonic functions (a)  $t_2^0(\theta, \phi)$  and (b)  $t_4^0(\theta, \phi)$  in Eq. (26) and the Wyckoff positions:  $8f$ ,  $8i$ ,  $8j$ , and  $2b$  in  $\text{SmFe}_{12}$  on the (010) and (110) plane.

For typical intermetallic compounds, it has been shown that the on-site and off-site contributions compete with each other, and the former is dominant, as in the case of  $\text{SmCo}_5$  [31] and  $\text{Nd}_2\text{Fe}_{14}\text{B}$  [55]. In these cases, for example, by combining the left panel of (a) and (b) with (c) for  $\text{SmCo}_5$  and  $\text{Nd}_2\text{Fe}_{14}\text{B}$ , respectively, we can understand the mechanism underlying uniaxial MA. Consequently, the stable direction of the magnetic moment, on a series of  $R^{3+}$ , is qualitatively determined by the ligand configuration.

The on-site and off-site contributions to the CF parameters can be quantized by decomposing Eq. (13) into the following form [31,44]:

$$A_l^m \langle r^l \rangle (\text{on}) = \frac{a_{l,m}}{2l+1} \frac{e^2}{\epsilon_0} \int_0^{r_{\text{As}}^R} dr r^2 |R_{4f}(r)|^2 \times \int_0^{r_{\text{As}}^R} dr' r'^2 \rho_l^m(r') \frac{r_{<}^l}{r_{>}^{l+1}}, \quad (24)$$

$$A_l^m \langle r^l \rangle (\text{off}) = A_l^m \langle r^l \rangle - A_l^m \langle r^l \rangle (\text{on}) \quad (25)$$

with

$$\rho_l^m(r) = \int_0^\pi d\theta \int_0^{2\pi} d\phi \sin^2 \theta \rho_{\text{rest}}^0(\mathbf{r}) t_l^m(\theta, \phi), \quad (26)$$

where  $\rho(\mathbf{r})$  is the electron density and  $r_{<} = \min(r, r')$  and  $r_{>} = \max(r, r')$ . In this study, Eqs. (24) and (25) will be referred to as the on-site and off-site contributions, respectively, which correspond roughly to the valence and lattice contributions.

### B. MA in the $\text{SmFe}_{12}$ compounds

As shown in Fig. 5, in  $\text{SmFe}_{12}$ , the nearest Fe is located at the  $i$  site and there is a vacancy at the  $2b$  site. Therefore, the orientation of a  $4f$  electron cloud, in the shape as shown in the left panel of (a), and the development of a uniaxial MA with  $K_1 > 0$  and  $K_2 < 0$  has been previously discussed, qualitatively [24]. When light elements are doped at the  $2b$  site, the electronic structure around the Sm ions changes and the MA is expected to be greatly affected. On the other hand, when Fe is substituted, the effect on the MA depends on the replacement site and the substituted atomic species. The effects of elemental doping and substitutions on MA were investigated as follows.

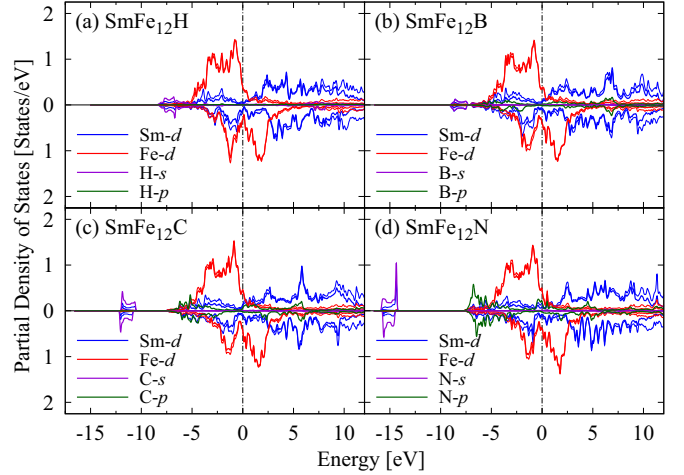


FIG. 6. Orbital projected partial density of states (PDOS) in  $\text{SmFe}_{12}X$  for  $X=(a)$  H, (b) B, (c) C, and (d) N, where the data is averaged for each inequivalent site of Fe ions. The PDOS of all orbitals for Sm and Fe are represented by thin solid lines. The Fermi level is set to zero.

## IV. ELECTRONIC STRUCTURE AND MODEL PARAMETERS IN $\text{SmFe}_{12}$ AFTER DOPING AND SUBSTITUTION

In this section, we present the results of the first-principle calculations of the electronic structure of  $\text{SmFe}_{12}X$  ( $X=\text{H, B, C, and N}$ ) and  $\text{SmFe}_{11}M$  ( $M=\text{Ti, V, and Co}$ ) and the model parameters used in the finite temperature calculations. Firstly, the partial density of states (PDOS) are shown in Figs. 6 and 9. The distributions of the charges and magnetic moments are shown in Tables I and III. Finally, the model parameters used to analyze the magnetic properties are shown in Tables II and IV, where the values of anisotropy constants  $k_1$  and  $k_2$  on Sm ions at absolute zero are also mentioned. To clarify the effect of the screened nuclear charge on the CF, the sum of the nuclear and electronic charges in the atomic sphere is shown as the charge at each site.

### A. Model parameters for $\text{SmFe}_{12}X$ ( $X=\text{H, B, C, and N}$ )

The PDOS in  $\text{SmFe}_{12}X$  ( $X=\text{H, B, C, and N}$ ) are shown in Fig. 6. The contribution of the  $3d$  and  $5d$  orbitals are dominant in the PDOS of Fe and Sm ion, respectively. Here, the  $4f$  electrons in the Sm ion are treated as core electrons, so their contribution does not appear in the PDOS. The energy positions of the  $s$  and  $p$  orbitals of  $X$  differ remarkably depending on the type of the light element. In the case of H addition, the  $1s$  orbital is located at the bottom of the density of states of Fe. In the case of B, C, and N doping, the weights of the  $s$  and  $p$  orbitals of the light elements shift to the lower-energy side, corresponding to an increase in the nuclear charge. For  $X=\text{B}$  and C, strong hybridization of Sm orbitals and  $X-s$  orbitals is observed around  $-11$  eV and  $-15$  eV, respectively.

The results of doping and substitution on the electronic structure of  $\text{SmFe}_{12}X$  ( $X=\text{B, C, and N}$ ) are shown in Table I. Firstly, in the material  $\text{SmFe}_{12}$ , the value of the charge and magnetic moment differs depending on the Fe inequivalent site. The magnetic moments of  $\text{Fe}(8i)$  and  $\text{Fe}(8f)$  exhibit the

TABLE I. Distribution of charges and magnetic moments on each site [Sm( $2a$ ), Fe( $8f$ ), Fe( $8i$ ), Fe( $8j$ ), and  $X(2b)$ ] and interstitial regions (int.) in SmFe<sub>12</sub> ( $M=n/a$ ) and SmFe<sub>12</sub> $X$  ( $X=H, B, C,$  and  $N$ ) compounds, where  $e$  and  $\mu_B$  denote the elementary charge and the Bohr magneton, respectively. The partial magnetization excluding the contribution of the  $4f$  electrons per two f.u. ( $VM^{TM}$ ) is also shown. These results were obtained using the first-principle calculations at absolute zero.

$X$	Charge ( $e$ )						Magnetic moment ( $\mu_B$ )						$VM^{TMa}$
	Sm( $2a$ ) <sup>a</sup>	Fe( $8f$ )	Fe( $8i$ )	Fe( $8j$ )	$X(2b)$	Int.	Sm( $2a$ ) <sup>a</sup>	Fe( $8f$ )	Fe( $8i$ )	Fe( $8j$ )	$X(2b)$	Int.	
$n/a$	5.82	1.25	1.42	1.34		-33.78	-0.50	1.90	2.56	2.32		-1.58	51.63
H	5.74	1.26	1.43	1.32	0.26	-34.05	-0.50	1.99	2.55	2.16	-0.02	-1.46	51.07
B	5.41	1.26	1.40	1.17	2.00	-35.44	-0.50	2.21	2.55	1.86	-0.08	-1.65	50.18
C	5.41	1.25	1.40	1.18	2.13	-35.80	-0.45	2.29	2.56	1.84	-0.10	-1.54	50.85
N	5.44	1.25	1.40	1.21	2.00	-35.79	-0.36	2.32	2.59	2.11	0.08	-1.37	54.19

<sup>a</sup>Excluding the contribution of the  $4f$  electrons.

largest and smallest value, respectively. These relations are the same as those obtained in a previous study for NdFe<sub>12</sub> [1]. The magnetic moment acting on an Sm ion, excluding the  $4f$  electrons, is mainly contributed by  $5d$  orbitals, which has the opposite sign to that of Fe.

Doping with a light element at the  $2b$  site causes the valence electrons bound by the  $X$  ions to be distributed in Sm( $2a$ ) and Fe( $8j$ ) adjacent to the  $2b$  site and in the interstitial region. Thus, it is confirmed that the positive charges of Sm( $2a$ ) and Fe( $8j$ ) decrease. Among them, the change in the electron density distribution is small when  $X=H$ . The partial magnetization  $VM^{TM}$  increases only in the case of nitrogeation. In this case, compared to  $X=B$  and  $C$ , the antibonding  $p$  orbitals are filled in the up-spin state as shown in Fig. 6(d), which leads to a sudden increase in partial magnetization  $VM^{TM}$ , where the magnetic moment of Fe( $8j$ ) adjacent to N( $2b$ ) decreases, while the magnetic moment of Fe( $8f$ ) increases significantly. This scenario has been discussed in detail using the simplified model by Harashima *et al.* [18] and the results are consistent with those of a previous study for NdFe<sub>12</sub>N compounds [1].

Table II shows the values of the CF parameters and the exchange field  $B_{ex}$  acting on the  $4f$  shell in the Sm ions of SmFe<sub>12</sub> $X$  ( $X=H, B, C$  and  $N$ ). In all cases, the contribution of  $A_2^0\langle r^2 \rangle$  is dominant. Therefore, from the sign of  $A_2^0\langle r^2 \rangle$ , it is qualitatively expected that the uniaxial and in-plane MA occurs in  $X=H$  and  $X=B, C,$  and  $N$ , respectively. The values of  $A_2^0\langle r^2 \rangle = -25$  K [19],  $-65$  K [20], and  $-32$  K [23] were obtained in previous studies. Among them,  $-65$  K obtained by the same open-core method as ours is the closest value. On the other hand, in the case of SmFe<sub>12</sub>N, our result of  $A_2^0\langle r^2 \rangle$

is 774.7 K, which is larger than the value of 244 K [20] and 249 K [23]. This discrepancy is thought to be caused by the lack of structural optimization in our calculations. Harashima *et al.* show that the volume expands due to nitriding. By taking this strain into account in our calculations, the hybridization of Sm and N sites is weakened, and the value of the CF  $A_2^0\langle r^2 \rangle$  is expected to be smaller. Each value of  $B_{ex}(0)$  is not related to the Fe spin density but is roughly proportional to the valence electron spin density at the Sm site shown in Table I. This is consistent with the mechanism proposed by Brooks *et al.* [50] and examined by Liebs *et al.* [52], where the exchange field originates from the intra-atomic  $4f$ - $5d$  coupling and no major contribution of nonlocal  $4f$ - $3d$  effective interaction persists, hence, our estimation of  $B_{ex}(0)$  is justified.

From these parameters, the MA constants  $k_1(0)$  and  $k_2^{(1)}(0)$  per Sm ion can be obtained analytically. The results are shown in columns 8 and 9. The MA constant  $k_1(0)$  differs depending on the doped element. Particularly, in the case of hydrogenation, the value of  $k_1(0)$  becomes about twice larger than that of SmFe<sub>12</sub>.

### B. Mechanism of MA in SmFe<sub>12</sub> $X$ ( $X=H, B, C,$ and $N$ )

Figure 7 shows the change in the charge density owing to the doping of light elements at the  $2b$  site, where an Sm ion is located in the middle of the figure.  $\Delta\rho(\mathbf{r})$  is defined as the charge density of SmFe<sub>12</sub> $X$  minus that of SmFe<sub>12</sub>. The common feature of the two is the increase in the electron density around the  $2b$  site due to the addition of a light element  $X$ . This increased electron density gets distributed inside the atomic sphere of Sm because the binding of the added element

TABLE II. CF parameters  $A_l^m\langle r^l \rangle$  [K] for ( $l, m$ ) and exchange field  $B'_{ex} = \mu_B B_{ex}(0)/k_B$  [K] obtained using the first-principle calculations in SmFe<sub>12</sub> ( $M=n/a$ ) and SmFe<sub>12</sub> $X$  ( $X=H, B, C,$  and  $N$ ) compounds, where  $\mu_B$  and  $k_B$  are the Bohr magneton and Boltzmann constant, respectively. First (second) order MA constant for a single Sm ion  $k_{1,2}^{(1)}(0)$  [K] at  $T=0$  K is also shown, which were analytically obtained using Eqs. (56) and (57) as given in Ref. [24].

$X$	(2,0)	(4,0)	(4,4)	(6,0)	(6,4)	$B'_{ex}$	$k_1$	$k_2$	$k_2^1$
$n/a^a$	-71.4	-21.3	-49.3	5.9	3.0	296.1	97.7	-40.9	-2.3
H	-163.7	-49.5	-6.7	3.9	3.2	294.3	220.1	-83.5	-0.4
B	172.2	-31.4	17.9	-13.4	8.6	292.3	-84.4	-34.1	0.5
C	439.0	-2.3	27.9	-8.1	12.0	261.3	-343.8	6.0	0.9
N	774.7	48.1	29.8	2.1	12.2	203.2	-683.5	72.2	1.0

<sup>a</sup>Previous calculation shown in Ref. [24].

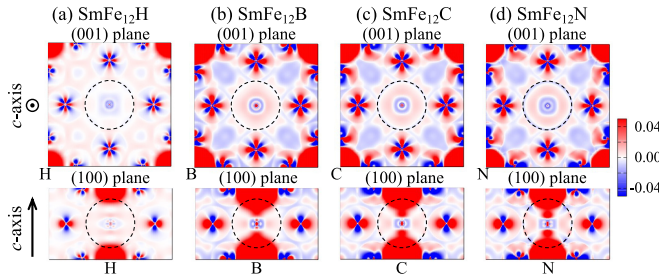


FIG. 7. Difference in the electron density  $\Delta\rho_0^0(r)$  [ $a_0^{-3}$ ] between  $\text{SmFe}_{12}X$  [ $X =$  (a) H, (b) B, and (c) N] and  $\text{SmFe}_{12}$ , where  $a_0$  is the Bohr radius. An Sm ion is located at the center of the figure and the dashed circles represent the atomic sphere radius  $r_{AS}^{\text{Sm}} = 3.2a_0$ .

$X$  is weak. As shown in the lower panel, in the case of (a)  $X=\text{H}$ , there is no significant change in the charge density near the Sm site. On the other hand, in the case of (b)–(d)  $X=\text{B}$ , C, and N, the change extends to the vicinity of the Sm site.

To clarify the effect of this charge density, change on the CF, Fig. 8(a) shows the distribution  $\Delta n_2^0$  of the electron density in the Sm  $2a$  site, which is defined by  $\Delta n_2^0 = \int_0^{r_{AS}^{\text{Sm}}} r^2 \rho_2^0(r) dr$ . Compared to the case of  $\text{SmFe}_{12}$ , the  $\Delta n_2^0$  changes to the opposite sign with the addition of light elements, indicating that the valence electrons on the Sm site are biased in the prolate shape along the  $c$  axis. Especially in the case of  $X=\text{B}$ , C, and N, the value of  $\Delta n_2^0$  is one order of magnitude larger.

The CF parameters decomposed into the on-site and off-site contributions [Fig. 8(b)] show that there is a strong correlation between the asphericity of charge density and  $A_2^0\langle r^2 \rangle(\text{on})$ . In the case of  $\text{SmFe}_{12}$  ( $X = n/a$ ), the on-site contribution is more dominant than the off-site one, indicating the occurrence of uniaxial MA [24]. Conversely, when a light element is added at the  $2b$  site, both the on-site and

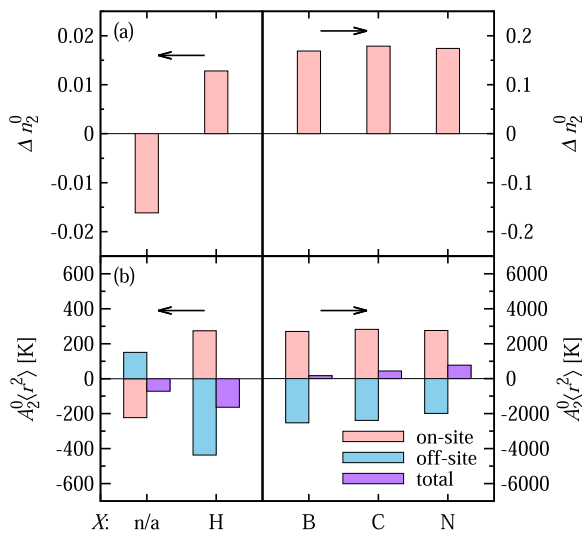


FIG. 8. (a) Asphericity of valence electron cloud defined by  $\Delta n_2^0 = \int_0^{r_{AS}^{\text{Sm}}} r^2 \rho_2^0(r) dr$  and (b) on-site and off-site contribution to  $A_2^0\langle r^2 \rangle$  on Sm site in  $\text{SmFe}_{12}$  ( $X = n/a$ ) and  $\text{SmFe}_{12}X$  ( $X = \text{H}$ , B, C, and N).

off-site contributions have opposite signs to those of  $\text{SmFe}_{12}$ . This reflects that the nearest neighbor ions to the Sm site are switched from the horizontal arrangement [Fig. 4(a)] to the vertical arrangement [Fig. 4(b)] on the addition of the light elements. Comparing the magnitude of the on-site and off-site contributions for each substitutional element, the off-site contribution is larger only for  $X=\text{H}$ . When H is added to the  $2b$  site, the change in the charge density near Sm is small and is largely affected by the positive nuclear charge. Therefore, the off-site contribution becomes dominant and  $A_2^0\langle r^2 \rangle(\text{on})$  becomes negative. Conversely, in the case of  $X=\text{B}$ , C, and N, the change in the charge density just above the Sm site is large and the valence contribution becomes more dominant than the lattice contribution, and the sign of  $A_2^0\langle r^2 \rangle$  becomes positive. In summary, for  $X=\text{H}$  the lattice contribution is dominant and exhibits a strong uniaxial MA, while for  $X=\text{B}$ , C, and N, the valence contribution is dominant and displays a strong in-plane anisotropy.

### C. Model parameters for $\text{SmFe}_{11}M$ ( $M=\text{Ti}$ , V, and Co)

The PDOS for  $\text{SmFe}_{11}M$  ( $M=\text{Ti}$ , V, and Co) is shown in Fig. 9. While the averaged PDOS for the inequivalent sites of Fe show a similar distribution, the PDOS for the substitutional elements are characteristic in their nature. In the case of  $M=\text{Ti}$  and V, the magnetic polarization is in a direction opposite to that of Fe, and in the case of  $M=\text{Co}$ , the polarization is in the same direction as that of Fe. In the case of Co substitution, the number of occupied electrons, especially in the minority band, increases. From these results, Ti and V are expected to have opposite magnetic moments with respect to Fe, while Co is parallel to Fe but with a decreasing magnitude.

Next, the charge and magnetic properties of  $\text{SmFe}_{11}M$  ( $M=\text{Ti}$ , V, and Co) is reported in Table III. Here, the numbers in parentheses denote the magnitude of the charge and spin moments of the substitution sites. First, we note the charge distribution. Regardless of the location of the substitution, when  $M=\text{Ti}$  or V, electron binding at the substitution site increases, and the electron density in the interstitial region increases. On the contrary, when  $M=\text{Co}$ , the amount of charge on the substitution site decreases slightly because Co attracts more electrons. Next, we focus on the magnetic moment. In the case of  $M=\text{Ti}$  or V, the substitution element has a magnetic moment that is antiparallel to Fe. As a result, the partial magnetization  $VM^{\text{TM}}$  is greatly reduced. On the other hand, when Fe is replaced by Co, the magnetic moment of Co itself decreases as indicated in the parenthesis, but the magnitude of the partial magnetization  $VM^{\text{TM}}$  increases or decreases depending on the substitution site, but the change is smaller than as that of element doping.

Similar to the case of element doping, the values of  $A_l^m\langle r^l \rangle$ ,  $B_{\text{ex}}(0)$  and the  $k_{1,2}^{(1)}(0)$  in  $\text{SmFe}_{11}M$  ( $M=\text{Ti}$ , V, and Co) are shown in Table IV. The CF parameters in each  $M$  exhibit variations depending on the substitution site even for the same substitution element. In particular, the value of  $A_2^0\langle r^2 \rangle$  is positive only when the Fe( $8i$ ) site is replaced by Ti. This has been confirmed in the previous study [20], which showed that the Fe( $8i$ ) site is preferentially replaced by Ti and the value of  $A_2^0\langle r^2 \rangle = 8$  K. This is consistent with our results that it takes



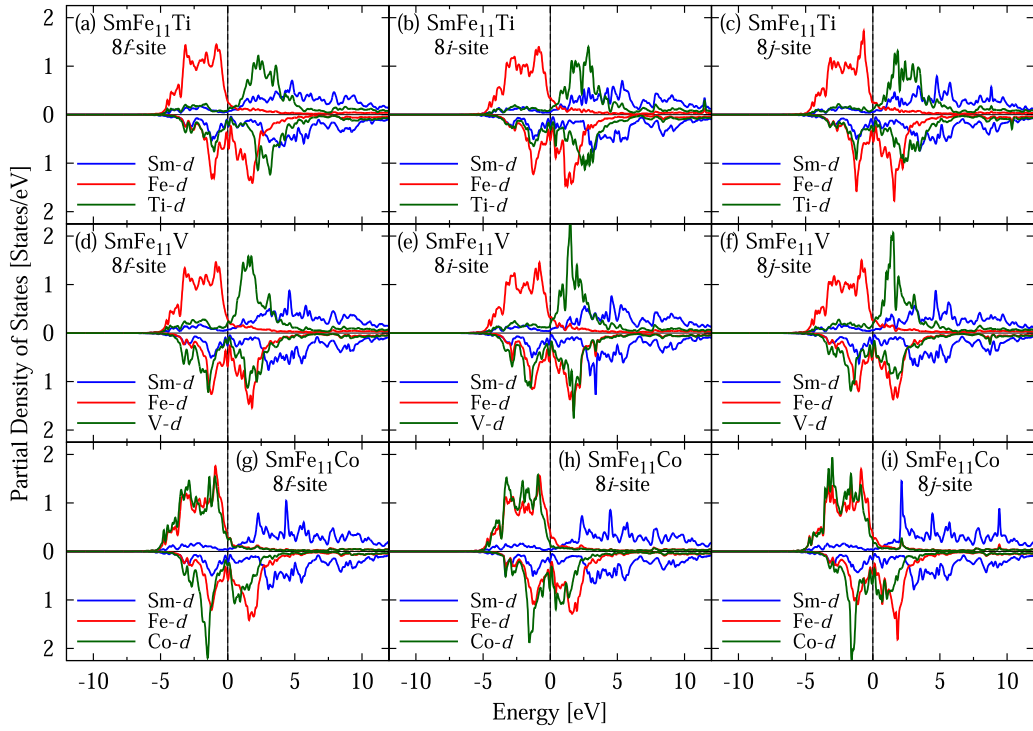


FIG. 9. Orbital projected partial density of states in  $\text{SmFe}_{11}M$  for  $M =$  (a)–(c) Ti, (d)–(f) V, and (g)–(i) Co for each replacement site, where the data is averaged for each ion. The Fermi level is set to zero.

a small positive value. On the other hand, the value of  $B_{\text{ex}}$  is almost the same regardless of the type of substitution, owing to the comparable spin moments of Sm (shown in Table II). Based on the values of the MA constants obtained from these parameters,  $k_1$  is always positive, regardless of the type of substitution.

The MA is significantly increased by substituting Ti and V with Fe(8*j*), and in the case of Co substitution, the MA increases irrespective of the location of the substituted site. However, when Fe(8*i*) is replaced by Ti, the uniaxial MA is greatly reduced because  $k_2(0)$  has a larger negative magnitude than  $k_1(0)$ . Note that for  $M = \text{Ti}_{8i}$ ,  $A_4^4(r^4)$  possesses a large value of  $-112.7$  K. This contributes to the in-plane MA

through  $k_2^1$ , as shown in Eq. (C5), however, due to the small  $A_4^4(r^4)$  coefficient, the value of  $k_2^1$  is small.

#### D. Mechanism of MA in $\text{SmFe}_{11}M$ ( $M = \text{Ti, V, and Co}$ )

Figure 10 shows the change in the charge density after elemental substitution. The substitution increases or decreases the screened nuclear charge and changes the charge density in the other regions. The screened nuclear charge acts directly on the 4*f* electron cloud as an electrostatic potential. Thus, a change in the screened nuclear charge at the substitution site is also important. The charges at the 8*f*, 8*i*, and 8*j* sites of Fe in  $\text{SmFe}_{12}$  are 1.25, 1.42, and 1.34, respectively. The change

TABLE III. Same as Table I but in  $\text{SmFe}_{11}M$  ( $M = \text{Ti, V, and Co}$ ) for each replacement site, which is indicated by the subscript to  $M$ . The columns of TM1, TM2, and TM3 show the averaged magnetic moments at the 8*f*, 8*i*, and 8*j* sites in the original  $\text{SmFe}_{12}$  and numbers in parenthesis denote the magnetic moment of the  $M$  ion.

$M$	Charge ( $e$ )					Magnetic moment ( $\mu_B$ )					$VM^{\text{TMa}}$
	Sm <sup>a</sup>	TM1	TM2	TM3	Int.	Sm <sup>a</sup>	TM1	TM2	TM3	Int.	
n/a	5.82	1.25	1.42	1.34	-33.78	-0.50	1.90	2.56	2.32	-1.58	51.63
$\text{Ti}_{8f}$	5.91	1.41(1.80)	1.45	1.37	-35.69	-0.52	1.30(-0.70)	2.49	2.34	-2.09	45.85
$\text{Ti}_{8i}$	5.94	1.28	1.58(1.97)	1.38	-35.79	-0.55	1.87	1.69(-0.72)	2.28	-2.21	43.39
$\text{Ti}_{8j}$	5.90	1.27	1.45	1.52(1.90)	-35.74	-0.55	1.90	2.48	1.59(-0.69)	-2.18	44.46
$\text{V}_{8f}$	5.91	1.39(1.72)	1.45	1.37	-35.49	-0.50	1.17(-1.27)	2.47	2.32	-2.06	44.64
$\text{V}_{8i}$	5.92	1.28	1.55(1.87)	1.38	-35.52	-0.54	1.87	1.48(-1.45)	2.26	-2.18	41.64
$\text{V}_{8j}$	5.90	1.27	1.45	1.49(1.80)	-35.49	-0.54	1.91	2.45	1.39(-1.39)	-2.18	42.75
$\text{Co}_{8f}$	5.87	1.24(1.15)	1.44	1.37	-34.12	-0.51	1.93(1.53)	2.60	2.44	-1.67	53.13
$\text{Co}_{8i}$	5.87	1.27	1.41(1.30)	1.37	-34.09	-0.52	1.98	2.37(1.74)	2.37	-1.66	51.06
$\text{Co}_{8j}$	5.87	1.27	1.44	1.33(1.23)	-34.11	-0.52	2.05	2.61	2.19(1.62)	-1.69	52.10

<sup>a</sup>Excluding the contribution of the 4*f* electrons.

TABLE IV. Same as Table II but in  $\text{SmFe}_{11}M$  ( $M = \text{Ti}, \text{V}, \text{and Co}$ ) for each replacement site, which is indicated by the subscript to  $M$ . CF parameters caused by local rotational symmetry breaking due to elemental substitution are shown in Table VI in Appendix D.

$M$	(2,0)	(4,0)	(4,4)	(6,0)	(6,4)	$B'_{\text{ex}}$	$k_1$	$k_2$	$k_2^1$
$n/a^a$	-71.4	-21.3	-49.3	5.9	3.0	296.1	97.7	-40.9	-2.3
$\text{Ti}_{8f}$	-49.8	-21.3	48.7	5.0	-3.2	301.5	80.2	-39.8	2.3
$\text{Ti}_{8i}$	19.9	-34.5	-112.7	6.0	-0.8	319.5	49.4	-61.0	-5.0
$\text{Ti}_{8j}$	-212.4	-13.6	-33.5	6.4	-17.3	319.6	192.5	-28.7	-1.0
$\text{V}_{8f}$	-57.1	-25.6	32.5	5.2	-5.8	285.1	94.2	-47.2	1.7
$\text{V}_{8i}$	-71.7	-29.5	-26.5	5.8	-4.6	317.1	111.7	-53.1	-1.0
$\text{V}_{8j}$	-211.2	-18.2	18.2	6.1	-17.0	316.6	199.9	-35.6	1.3
$\text{Co}_{8f}$	-78.9	-22.6	-32.7	5.9	-0.5	301.4	105.7	-42.9	-1.5
$\text{Co}_{8i}$	-120.4	-18.0	4.2	5.5	-2.4	304.5	129.4	-35.0	0.3
$\text{Co}_{8j}$	-94.3	-23.1	-25.8	5.4	2.1	306.3	118.1	-42.9	-1.2

<sup>a</sup>Previous calculations are presented in the Ref. [24].

in the screened nuclear charge of the substituted ions is shown by the numbers under the  $X$  symbol.

Since the charge density difference  $\Delta\rho(\mathbf{r})$  shows a complicated distribution, it is shown together with the distribution

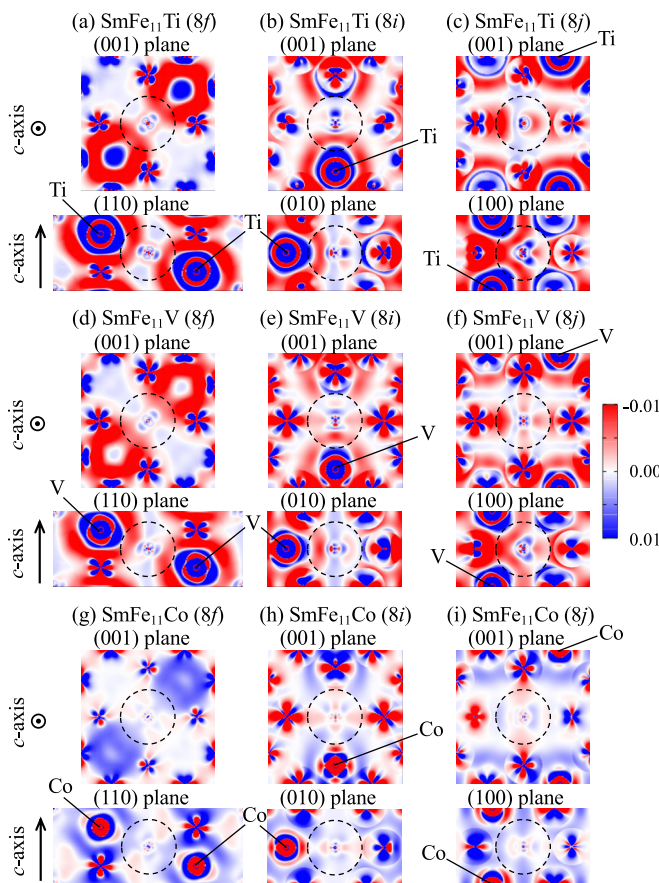


FIG. 10. Difference in the electron density  $\Delta\rho_{\text{rest}}^0(\mathbf{r})$  [ $a_0^{-3}$ ] and screened nuclear charge [ $e$ ], which is shown below the symbols  $M$ , between  $\text{SmFe}_{11}M$  [ $M = \text{(a)–(c) Ti, (d)–(f) V, and (g)–(i) Co}$ ] and  $\text{SmFe}_{12}$  with substitution for each Fe 8 $f$ , 8 $i$ , and 8 $j$  site in  $\text{SmFe}_{12}$ . An Sm ion is located at the center of the figures and the dashed circles represent the atomic sphere radius  $r_{\text{AS}}^{\text{Sm}} = 3.2a_0$ . In order to measure the difference, the crystal structure of  $\text{SmFe}_{12}$  is adjusted to each one of  $\text{SmFe}_{11}M$ .

parameter shown in Fig. 11(a). Originally, the valence electrons at the Sm site have an oblate shape. Since the sign of  $\Delta n_2^0$  does not change with elemental substitution, it can be seen from Fig. 11(a) that an oblate shape similar to the one in  $\text{SmFe}_{12}$  is realized.

It can be seen in Fig. 10 that both the positive nuclear charge at each substitution site and the electron density increases for a Ti and V substitution and decreases for a Co substitution. However, since the charge density difference shows a complicated distribution, we confirm the asphericity of the valence electron cloud in  $\Delta n_2^0$  as shown in Fig. 11(a). Originally, the valence electron of the Sm site in  $\text{SmFe}_{12}$  has an oblate shape ( $\Delta n_2^0 < 0$ ). Since the sign of  $\Delta n_2^0$  does not change even after an elemental substitution, a similar oblate shape of the valence electron cloud as that of  $\text{SmFe}_{12}$  is realized.

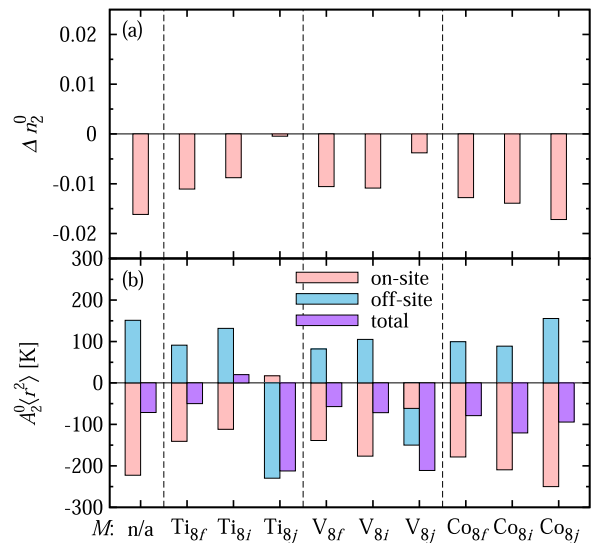


FIG. 11. (a) Asphericity of valence electron cloud defined by  $\Delta n_2^0 = \int_0^{r_{\text{AS}}^{\text{Sm}}} r^2 \rho_2^0(r) dr$  and (b) on-site and off-site contribution to  $A_2^0(r^2)$  at the Sm site in  $\text{SmFe}_{12}$  ( $M = n/a$ ) and  $\text{SmFe}_{11}M$  ( $M = \text{Ti}, \text{V}, \text{and Co}$ ) for each replacement site, which is indicated by the subscript to  $M$ .

In the following section, we discuss the results of a detailed investigation of the substitution of light, i.e., Ti and V and heavy, i.e., Co elements, separately. As shown in Fig. 10, when Fe is substituted for Ti and V, the weak positive charge of the nucleus weakens the electron binding, resulting in an increase in the screened nuclear charge and the electron density in the interstitial region. Consequently, the asphericity decreases in both the cases of Ti and V substitution. In particular, when Fe(8*j*) is substituted for Ti and V,  $\Delta n_2^0$  decreases significantly. This is probably due to the increase in the charge density near the 8*j* substitution site, as shown in the lower panels of Figs. 10(c) and 10(f). Next, we focus on the effect of the charges outside the atomic sphere on  $A_2^0(r^2)$ (off-site) and clarify the mechanism that determines the total  $A_2^0(r^2)$ . When the Fe at the 8*j* site is replaced by Ti or V, the positive charge at the site increases, and the 4*f* electrons of Sm shown in the right panel of Fig. 4(b) are stabilized in a prolate shape with respect to the *c* axis. In fact, from the configuration between the 8*j* site of Sm, as shown in Fig. 5(a), the off-site contribution  $A_2^0(r^2)$ (off) and the total  $A_2^0(r^2)$  attains a large negative magnitude, as shown in Fig. 11(b). However, when one of the 8*i* sites adjacent to Sm is substituted with Ti or V, the off-site contribution is positively larger than that of the other substitution sites. Especially in the case of Ti substitution, where the increase in the positive charge is large, the prolate orientation of 4*f* electrons is stabilized. This is reflected in the positive value of the total  $A_2^0(r^2)$ , as shown in Fig. 11(b).

In the case of Co substitution, the positive charge of the screened nucleus and the electron density in the interstitial region decrease because of the attraction of the large positive charge of Co ions to electrons. In particular, the electron density in the *c*-axis direction from Sm to the 2*b* site, in the presence of a void, is reduced regardless of the substitution site. This can be confirmed by the profiles of the lower panel depicted in Figs. 10(g)–10(i). Hence, value of the total  $A_2^0(r^2)$  decreases as shown in Fig. 11(b). As a result, the prolate 4*f* electron cloud tends to strongly fix along the *c*-axis direction, and subsequently the MA increases.

When Fe(8*j*) located above and along the *c* axis of Sm is replaced by Ti or V, the MA greatly increases owing to the effect of the shielded positive charge. Conversely, when Fe(8*i*) located laterally along the *a* or *b* axis of Sm is replaced by Ti, the MA changes from uniaxial to in-plane due to the influence of the screened positive charge. When Fe is replaced by Co, the MA increases independent of the substitution site. This occurs owing to a decrease in the charge density along the *c* axis from Sm and the fixing of the Sm 4*f* electron cloud along the direction of the *c* axis.

## V. CHANGES IN THE MACROSCOPIC MAGNETIC PROPERTIES IN $\text{SmFe}_{12}$ AS A RESULT OF DOPING AND SUBSTITUTION

The changes in the magnetic properties of  $\text{SmFe}_{12}X$  ( $X=\text{H, B, C, and N}$ ) and  $\text{SmFe}_{11}M$  ( $M=\text{Ti, V, and Co}$ ) are discussed in subsections A and B, respectively. The MA of  $\text{SmFe}_{12}$  is observed to change drastically as a result of doping and substitution, as summarized in Tables II and IV. In order to clarify the cause of the variation, the change in the charge distribution due to doping and substitution is illustrated, and

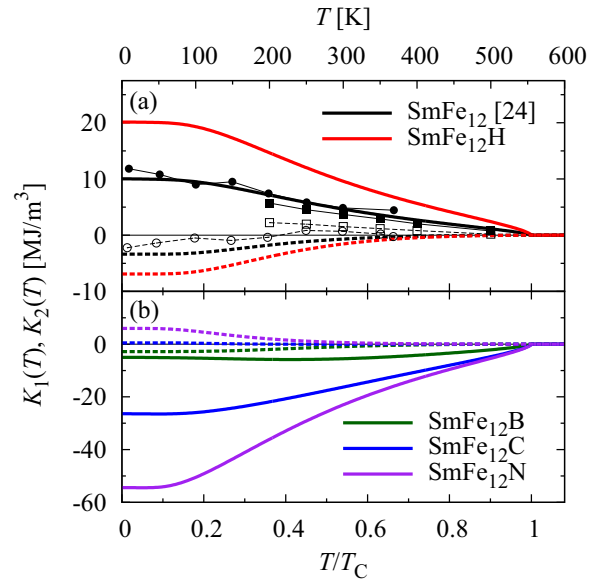


FIG. 12. Temperature-dependent MA constants  $K_1(T)$  (solid lines) and  $K_2(T)$  (broken lines) [ $\text{MJ}/\text{m}^3$ ] in (a)  $\text{SmFe}_{12}$  [24] and  $\text{SmFe}_{12}X$  [ $X =$  (a)H and (b) B, C, and N] compounds, where temperature is scaled using the Curie temperature  $T_C$ . These results were obtained by using the analytical method in Eqs. (21) and (22) as mentioned in Ref. [24]. The experimental results for  $K_1(T)$  and  $K_2(T)$  in  $\text{SmFe}_{12}$  are represented by solid and open plots, respectively, where the circles and squares represent the results measured in different experiments of the Sucksmith-Thompson method [9] and the anomalous Hall effect [13], respectively. Actual value of temperature for  $\text{SmFe}_{12}$  ( $T_C = 555$  K) is shown on the top of the graph.

the results of decomposing the CF  $A_2^0(r^2)$  of Sm into on-site and off-site contributions are also presented. On the other hand, the temperature dependence of the magnetization is mainly determined by the transition-metal elements, which accounts for most of the magnetization. In the present study, this is treated phenomenologically except for the values at absolute zero, and the temperature dependence of the magnetization of the whole system is not considerably different from Fig. 3. In fact, the magnetic moment carried by the 4*f* electrons in Sm is as small as  $0.3 \mu_B$  per atom [24]. Finally, the MA constants and magnetization curves at finite temperatures are shown.

### A. MA constants and magnetization curves in $\text{SmFe}_{12}X$ ( $X=\text{H, B, C, and N}$ )

We clarify the mechanism underlying the MA using the charge density distribution. Finally, we show the results of  $K_1$  and  $K_2$  at finite temperatures. The results for the finite temperature MA constants  $K_1$  and  $K_2$  calculated by using the analytical expressions in Eqs. (C3) and (C4) are shown in Fig. 12. Here, the horizontal axis represents the temperature scaled using the Curie temperature  $T_C$ . At all temperatures, the absolute value of  $K_1$  is larger than that of  $K_2$ . Next, we focus on the temperature dependence. According to Eq. (C3),  $A_2^0(r^2)$  and  $A_4^0(r^4)$  contribute to  $K_1$  with the same sign, and it is known that the terms containing higher order CF parameters with a high number of *l* decay quickly with increasing tem-

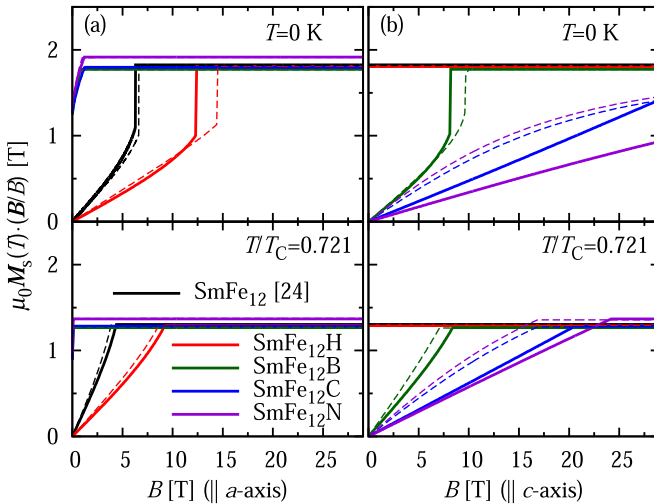


FIG. 13. Magnetization curves along the (a)  $a$  axis and (b)  $c$  axis at  $T=0$  and  $T/T_c=0.721$  in  $\text{SmFe}_{12}$  and  $\text{SmFe}_{12}X$  [ $X = \text{H}, \text{B}, \text{C}$  and  $\text{N}$ ] compounds. These results are obtained by using the analytical method in Eq. (63) mentioned in Ref. [24]. The thin broken curves show the statistical results obtained from Eq. (25) given in Ref. [24].

perature. In the case of  $\text{SmFe}_{12}$  and  $\text{SmFe}_{12}X$  of  $X=\text{H}$  and  $\text{N}$ ,  $A_2^0\langle r^2 \rangle$  and  $A_4^0\langle r^4 \rangle$  have the same sign and exhibit a monotonic temperature dependence. On the contrary, for  $\text{SmFe}_{12}X$  of  $X=\text{B}$  and  $\text{C}$ , they are opposite in signs, and especially for  $\text{SmFe}_{12}\text{B}$ , they exhibit a nonmonotonic temperature dependence. This is due to the fact that the  $A_4^0\langle r^2 \rangle$  term, which contributes positively to  $K_1$ , decays quickly with temperature. For  $X=\text{H}$ , the MA is increased by a factor of about 2 in  $K_1$ , which is expected to improve the magnetic properties. However, when light elements  $\text{C}$ , and  $\text{N}$  are added, strong in-plane anisotropy is observed due to the large positive value of  $A_2^0\langle r^2 \rangle$ .

Figure 13 shows the magnetization curve obtained analytically within the framework of the linear theory for the CF. Here we also show the results calculated by the statistical method Using the exact diagonalization, as shown by broken curves. (a) and (b) show the results when the magnetic field is applied in the  $a$ - and  $c$ -axis directions, respectively. (a) and (b) together exhibit a uniaxial MA in the case of  $\text{SmFe}_{12}$  and  $\text{SmFe}_{12}\text{H}$ , and an in-plane anisotropy in the case of  $\text{SmFe}_{12}X$  for  $X=\text{B}, \text{C}$ , and  $\text{N}$ . In particular, comparing  $\text{SmFe}_{12}$  and  $\text{SmFe}_{12}\text{H}$ , we can see that the MA is enhanced by hydrogenation. Moreover, the first-order magnetization process (FOMP) occurs at low temperatures. This can be deduced from the competition between the MA constants  $K_1(T)$  and  $K_2(T)$ . In fact, the FOMP condition  $-K_2(T) < K_1(T) < -6K_2(T)$  [24] is satisfied in this case. The strong in-plane anisotropy is observed for  $X=\text{C}$  and  $\text{N}$ . In this case, the difference between the results calculated by the analytical (solid curves) and statistical (broken curves) methods becomes large. This means that the framework of the linear approximation for CF is broken because the value of the  $A_2^0\langle r^2 \rangle$  is too large. For this reason, quantitiveness cannot be guaranteed in the case of  $X=\text{N}$  and  $\text{C}$ , and it is necessary to review the results using the first-principle calculations. However, qualitatively,

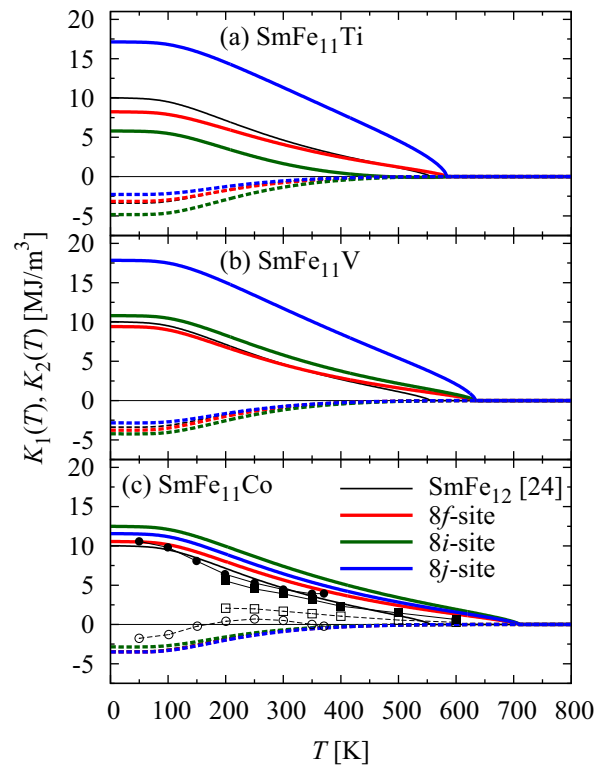


FIG. 14. Temperature-dependent MA constants  $K_1(T)$  (solid lines) and  $K_2(T)$  (broken lines) [ $\text{MJ}/\text{m}^3$ ] in  $\text{SmFe}_{12}$  and  $\text{SmFe}_{11}M$  [ $M = \text{(a) Ti, (b) V, and (c) Co}$ ] compounds for each replacement site. These results are obtained using the analytical method for Eqs (21) and (22), mentioned in Ref. [24]. The experimental results for  $K_1(T)$  and  $K_2(T)$  in  $\text{Sm}(\text{Co}_x\text{Fe}_{1-x})_{12}$  are represented by solid and open plots, respectively, where the circles and squares represent the results for  $\text{SmFe}_{11.16}\text{Co}_{0.84}$  using the Sucksmith-Thompson measurements [9] and for  $\text{SmFe}_{10.8}\text{Co}_{1.2}$  measured using the anomalous Hall effect [13].

it can be understood that the system exhibits a strong in-plane anisotropy.

## B. MA constants and magnetization curves in $\text{SmFe}_{11}M$ ( $M = \text{Ti, V, and Co}$ )

The calculated MA constants  $K_1$  and  $K_2$  at finite temperatures are shown in Fig. 14. At all temperatures,  $K_1$  is positive and  $K_2$  is negative. In case of substitution at the  $8f$  site, which is the farthest from  $\text{Sm}$ , the influence of the  $4f$  electron cloud is negligible. As a result, the temperature dependence is almost the same as that of the curve for  $\text{SmFe}_{12}$ , regardless of the type of the substituting element. This is consistent with the fact that a series of CF parameters and exchange fields have similar values. Conversely, when  $\text{Fe}(8j)$  is replaced by  $\text{Ti}$  or  $\text{V}$ ,  $A_2^0\langle r^2 \rangle$  takes a much larger value, and the rate of decrease of  $K_1$  with an increasing temperature is small. This results from the fact that the generalized Brillouin function  $B_l^j(x)$  and the  $T_l^j(x)$  function decrease more slowly with a smaller  $l$  [24]. On the contrary, when  $\text{Fe}(8i)$  is replaced by  $\text{Ti}$ , the rate of decrease of  $K_1$  with an increasing temperature increases owing to the small value of  $A_2^0\langle r^2 \rangle$ . Since,  $K_2$  does not include the contribution of  $A_2^0\langle r^2 \rangle$ , as shown in Eq. (C4),

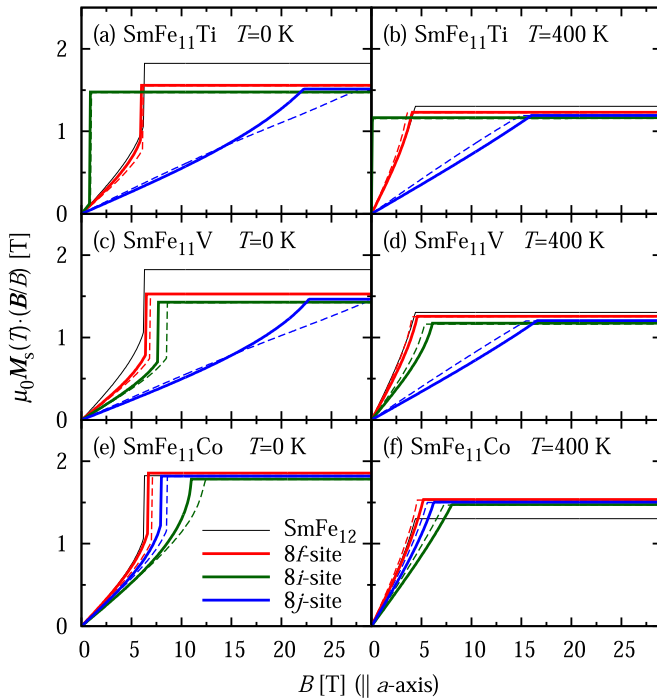


FIG. 15. Magnetization curves along the  $a$  axis at  $T = 0$  K and 400 K in  $\text{SmFe}_{11}M$  [ $M =$  (a), (b) Ti, (c), (d) V, and (e), (f) Co] compounds for each replacement site. These results are obtained by using the analytical method in Eq. (63) mentioned in the Ref. [24]. The thin broken curves show the statistical results obtained from Eq. (25) given in Ref. [24].

the  $K_2$  exhibits a negative temperature dependence in all cases and decays faster than  $K_1$ .

Similar to Fig. 13, Fig. 15 shows the magnetization curve in the case of  $\text{SmFe}_{11}M$  ( $M = \text{Ti, V, and Co}$ ). Here we present the results for the case where the magnetic field is applied along the  $a$  axis. Subsequently, there is a jump in the magnetization process for compounds that satisfy the FOMP condition at low temperatures. When Fe(8*f*) is replaced by a transition-metal element, the magnetization curve is similar to that of  $\text{SmFe}_{12}$ . The values of the FOMP field ( $T = 0$  K) and the anisotropic field ( $T = 400$  K) are also close to those of  $\text{SmFe}_{12}$ . This is a consequence of the 8*f* site being the farthest Fe site from the Sm site as shown in Fig. 5. However, the strong attraction of the rugbyballlike 4*f* electron cloud to the screened nuclear charge, as seen in the electronic structure analysis in Sec. IV C, results in a significantly enhanced MA when Fe(8*j*) is substituted with Ti or V. The large MA field of  $H_A \sim 16$  T is observed even at  $T = 400$  K because the decrease in the MA with an increasing temperature is slowed down by the large value of  $A_2^0(r^2)$ . Although, when Fe(8*i*) is replaced by Ti, FOMP is observed at low temperatures and small applied fields, and changes to an in-plane anisotropy at  $T = 400$  K with a zero field. This is consistent with the results shown in Fig. 14 from  $K_{1,2}(0) = 5.80, -4.83$  MJ/m<sup>3</sup> to  $K_{1,2}(400) = 0.45, -0.47$  MJ/m<sup>3</sup>. In the case of Co substitution, both the FOMP and MA fields exceed those of  $\text{SmFe}_{12}$ , regardless of the replacement site. Moreover, due to the large  $T_C$ , the saturation magnetization of  $\text{SmFe}_{11}\text{Ti}$  exceeds that of  $\text{SmFe}_{12}$  at  $T = 400$  K. The magnetization curves, i.e., the dashed curves,

produced using the statistical method, are in good agreement with the present results, and thereby, confirm that the analysis of  $\text{SmFe}_{11}M$  is plausible within the framework of the linear theory of CF. The additional CF parameters have also been accounted for in the statistical calculations, as shown in Table VI. The details are presented in Appendix D. The results show that the effect of the breaking of local symmetry on the macroscopic magnetization curve is small under the action of strong exchange fields.

## VI. SUMMARY

In this paper, the effect of element doping and substitution on the bulk magnetic properties of  $\text{SmFe}_{12}$  compounds was studied by analyzing the electronic structure. The crystal fields, exchange fields, and magnetic moments were determined from the first-principle calculations, and consequently, an effective spin model was developed. The macroscopic magnetic properties of these  $\text{SmFe}_{12}$  compounds were investigated using this model. The crystal field of the 4*f* electrons, generated due to the valence electron cloud and the screened nuclear charge, was investigated in detail, and the mechanism underlying the enhancement of the magnetic properties was clarified. We found that the first-order MA constant  $K_1$  increases approximately by a factor of two when hydrogen is added to the 2*b* site and when Fe(8*j*) is replaced by Ti or V. Moreover, we found that the decay of  $K_1$  with an increasing temperature is slower than that in the other cases because  $A_2^0$  has a particularly large value. This increase in the MA is realized by the attraction of the rugbyballlike 4*f* electron cloud to the shielded positive charge of the nucleus. The temperature dependence of  $K_1(T)$  and  $K_2(T)$  in  $\text{SmFe}_{11}\text{Co}$  was found to qualitatively reproduce the experimental results for  $\text{Sm}(\text{Fe}_{1-x}\text{Co}_x)_{12}$  ( $x = 0.1, 0.07$ ). Finally, the macroscopic magnetization curves were obtained from the electronic states within the first order of the crystal field. Consequently, we found that the first-order magnetization process often appears in many  $\text{SmFe}_{12}$ -based compounds with a uniaxial MA that satisfy the condition  $-K_2 < K_1 < -6K_2$  at low temperatures. Indeed, the compounds  $\text{SmFe}_{12}$ ,  $\text{SmFe}_{12}\text{H}$ ,  $\text{SmFe}_{11}\text{Ti}_{8f}$ ,  $\text{SmFe}_{11}\text{Ti}_{8i}\text{SmFe}_{11}\text{V}_{8f}$ ,  $\text{SmFe}_{11}\text{V}_{8i}$ ,  $\text{SmFe}_{11}\text{Co}_{8f}$ , and  $\text{SmFe}_{11}\text{Co}_{8j}$  depicted the first-order magnetization process in our calculations, where the replacement site is indicated by the subscript. We confirmed that this scheme works well except for the case of  $\text{SmFe}_{12}\text{C}$  and  $\text{SmFe}_{12}\text{N}$ .

## ACKNOWLEDGMENTS

This work was supported by ESICMM Grant No. 12016013 and ESICMM is funded by Ministry of Education, Culture, Sports, Science and Technology (MEXT). T.Y. was supported by JSPS KAKENHI Grant No. JP21K04625. P.N. was supported by the project Solid21. Part of the numerical computations were carried out at the Cyberscience Center, Tohoku University, Japan.

## APPENDIX A: HAMILTONIAN OF A SINGLE R ION WITH THE LS COUPLING SCHEME

Here, we apply the  $LS$  coupling scheme to the single  $R$  Hamiltonian in Eq. (2) owing to the strong Coulomb interac-

TABLE V. Comparison of the total energy in  $\text{SmFe}_{11}M$  ( $M=\text{Ti, V, and Co}$ ) for each replacement site, which is indicated by the subscript to  $M$ .

$M$	Total Energy (Ry)	$M$	Total energy (Ry)	$M$	Total energy (Ry)
$\text{Ti}_{8f}$	-101157.15591928	$\text{V}_{8f}$	-101539.19642501	$\text{Co}_{8f}$	-103315.78997575
$\text{Ti}_{8i}$	-101157.27273233	$\text{V}_{8i}$	-101539.25199749	$\text{Co}_{8i}$	-103315.77202788
$\text{Ti}_{8j}$	-101157.19639031	$\text{V}_{8j}$	-101539.20114312	$\text{Co}_{8j}$	-103315.78487875

tion between the  $4f$  electrons. According to the Hund's rule for trivalent  $R$  ion, we specify the quantum number of total orbital and spin moment  $L$  and  $S$  for operators  $\sum_{i=1}^{n_{4f}} \hat{s}_i = \hat{S}$  and  $\sum_{i=1}^{n_{4f}} \hat{l}_i = \hat{L}$ , respectively. The total angular momentum  $J$  is varied from  $|L - S|$  to  $L + S$ , and  $M$  is the magnetic quantum number. Thus the single ion Hamiltonian in Eq. (2) can be given as [30,42]:

$$\hat{H}_R = \lambda \hat{S} \cdot \hat{L} + 2\mu_B \hat{S} \cdot \mathbf{B}_{\text{ex}}(T) + \sum_{l,m} \frac{A_l^m \langle r^l \rangle}{a_{l,m}} \Theta_l^l t_l^m(\hat{L}) + \mu_B (\hat{L} + \hat{S}) \cdot \mathbf{B}, \quad (\text{A1})$$

where each term corresponds to  $\hat{H}_{\text{so}}$ ,  $\hat{H}_{\text{ex}}$ ,  $\hat{H}_{\text{CF}}$ , and  $\hat{H}_Z$ , respectively. Their corresponding basis can be written in the Russell-Saunders states  $|L, S; J, M\rangle$ . As for the spin-orbit interaction  $\lambda$  in Sm ions, we use an experimental value of  $\lambda/k_B = 411$  K [56]. In the  $\hat{H}_{\text{CF}}$  term we use the following equivalent relation [24,57]

$$\sum_{i=1}^{n_{4f}} t_l^m(\hat{\theta}_i, \hat{\phi}_i) = \Theta_l^l t_l^m(\hat{L}), \quad (\text{A2})$$

with the factor:

$$\Theta_l^L = 2^l \sqrt{\frac{(2L-l)!}{(2L+l+1)!}} \langle L \parallel \sum_{i=1}^{n_{4f}} C^{(l)}(\hat{\theta}_i, \hat{\phi}_i) \parallel L \rangle, \quad (\text{A3})$$

and operators:

$$t_l^{\pm|m|}(\hat{L}) = \sqrt{\pm \frac{2l+1}{8\pi}} [C_{-|m|}^{(l)}(\hat{L}) \pm (-1)^m C_{|m|}^{(l)}(\hat{L})], \quad (\text{A4})$$

$$t_l^0(\hat{L}) = \sqrt{\frac{2l+1}{4\pi}} C_0^{(l)}(\hat{L}), \quad (\text{A5})$$

for  $m \neq 0$  and  $m = 0$ , respectively. In the treatment of  $\hat{H}_{\text{so}}$ , we should note that because the  $LS$  coupling in Sm compounds is weak compared with the other  $R$  ones, the excited  $J$  multiplets must be included [24,32,33,37–39].

## APPENDIX B: COMPARISON OF TOTAL ENERGY IN $\text{SmFe}_{11}M$ ( $M=\text{TI, V, AND CO}$ )

In this section, we present the results in Table V showing the total energy per two f.u. The most stable substitution sites were found to be  $8i$ ,  $8i$ , and  $8f$  sites for Ti, V, and Co substitutions, respectively. In the case of Co substitution, the energy difference between  $8f$  and  $8j$  site substitutions was found to be small, approximately 5.097 mRy/2f.u. These results are consistent with the previous study [40].

## APPENDIX C: ANISOTROPY CONSTANTS FOR TETRAGONAL SYMMETRY

According to the analytical method, using the modified effective lowest  $J$ -multiplet Hamiltonian, the MA energy for the  $j$ th  $R$  can be written explicitly in the form [24]:

$$f_{\text{CF},j}(\mathbf{M}_s, T) = \sum_{l,m} A_{l,j}^m \langle r^l \rangle \Xi_l^J \frac{t_l^m(\Theta, \Phi)}{a_{l,m}} \times \left[ J^l B_j^l(x_j) + \frac{l(l+1)}{2l+1} T_j^l(x_j) \right], \quad (\text{C1})$$

with  $x_j = -J(g_j - 1)\mu_B B_{\text{ex},j}(T)/k_B T$ , where  $B_{\text{ex},j}$  denotes the exchange field acting on a  $4f$  shell in the  $j$ th Sm and  $g_j$  is Landé  $g$  factor.  $B_j^l(x_j)$  is the generalized Brillouin function [39,58] and  $T_j^l(x_j)$  is the function defined by Eq. (50) in Ref. [24]. The equivalent factor  $\Xi_l^J$  in Eq. (C1) was introduced in Ref. [24] and can be written in the form:

$$\Xi_l^J = 2^l \sqrt{\frac{(2J+1)(L+1)}{S}} \sqrt{\frac{(2J+l+2)(2J-l+1)!}{l(l+1)(2J+l+1)!}} \times \left\{ \begin{matrix} L & J & S \\ J+1 & L & l \end{matrix} \right\} \langle L \parallel \sum_{i=1}^{n_{4f,j}} C^{(l)}(\hat{\theta}_i, \hat{\phi}_i) \parallel L \rangle. \quad (\text{C2})$$

By comparing  $f_{\text{CF},j}(\mathbf{M}_s, T) - f_{\text{CF},j}(\mathbf{M}_s, \mathbf{n}_c, T)$  in Eq. (C1) with first term on the right-hand side of Eq. (21), the following MA constants with a fourfold rotational symmetry for trivalent magnetic light  $R$  ion ( $\text{Ce}^{3+}$ ,  $\text{Pr}^{3+}$ ,  $\text{Nd}^{3+}$ ,  $\text{Pm}^{3+}$ , and  $\text{Sm}^{3+}$ ) can be written as follows:

$$k_1(T) = -3[J^2 B_j^2(x) + \frac{6}{5} T_j^2(x)] A_2^0 \langle r^2 \rangle \Xi_2^J - 40[J^4 B_j^4(x) + \frac{20}{9} T_j^4(x)] A_4^0 \langle r^4 \rangle \Xi_4^J - 168[J^6 B_j^6(x) + \frac{42}{13} T_j^6(x)] A_6^0 \langle r^6 \rangle \Xi_6^J, \quad (\text{C3})$$

$$k_2(T) = 35[J^4 B_j^4(x) + \frac{20}{9} T_j^4(x)] A_4^0 \langle r^4 \rangle \Xi_4^J + 378[J^6 B_j^6(x) + \frac{42}{13} T_j^6(x)] A_6^0 \langle r^6 \rangle \Xi_6^J, \quad (\text{C4})$$

$$k_2^1(T) = [J^4 B_j^4(x) + \frac{20}{9} T_j^4(x)] A_4^4 \langle r^4 \rangle \Xi_4^J + 10[J^6 B_j^6(x) + \frac{42}{13} T_j^6(x)] A_6^4 \langle r^6 \rangle \Xi_6^J, \quad (\text{C5})$$

$$k_3(T) = -231[J^6 B_j^6(x) + \frac{42}{13} T_j^6(x)] A_6^0 \langle r^6 \rangle \Xi_6^J, \quad (\text{C6})$$

$$k_3^1(T) = -11[J^6 B_j^6(x) + \frac{42}{13} T_j^6(x)] A_6^4 \langle r^6 \rangle \Xi_6^J. \quad (\text{C7})$$

## APPENDIX D: SYMMETRY OPERATIONS ON $\text{SmFe}_{11}M$ ( $M=\text{TI, V, AND CO}$ )

Elemental substitutions locally break the fourfold rotational symmetry, which is considered to be recovered in the

TABLE VI. Crystal field parameters  $A_{l,1}^m(r^l)$  [K] for  $(l, m)$  without a fourfold rotational symmetry in  $\text{SmFe}_{11}M$  ( $M = \text{Ti, V, and Co}$ ) for each replacement site, which is indicated by the subscript to  $M$ .

system	(2, ±1)	(2, −2)	(2, 2)	(4, ±1)	(4, −2)	(4, 2)	(4, ±3)	(6, ±1)	(6, −2)	(6, 2)	(6, ±3)	(6, ±5)	(6, −6)	(6, 6)
Ti <sub>8f</sub>	±25.5	88.9		±57.0	−24.7		110.8	±5.4	−5.4		−11.1	±41.9	−13.4	
Ti <sub>8i</sub>			−320.8			52.7				−5.3				−10.4
Ti <sub>8j</sub>			164.2			138.8				9.5				0.8
V <sub>8f</sub>	±35.2	80.2		±24.4	−18.6		57.1	±3.8	−3.3		−7.7	±27.1	−8.7	
V <sub>8i</sub>			−285.1			28.5				−3.7				−8.8
V <sub>8j</sub>			146.5			74.7				6.9				1.4
Co <sub>8f</sub>	±124.6	80.7		±7.0	−3.5		13.8	±1.4	1.4		2.2	±12.5	3.4	
Co <sub>8i</sub>			−42.1			−21.3				0.8				1.7
Co <sub>8j</sub>			36.0			−29.5				−2.8				1.0

whole system. In this section, we describe the procedure to calculate the bulk magnetic properties from the CF parameters obtained using the first-principle calculations for the specific structure shown in Figs. 2(b)–2(d), in which the complete set of CF parameters include the contribution shown in Table VI. The Hamiltonian for a system satisfying a fourfold rotational symmetry can be written in general as:

$$\hat{\mathcal{H}} = \frac{1}{4} \sum_{k=1}^4 \sum_{j=1}^{n_R} e^{i\hat{L}_z \pi (k-1)/2} \hat{\mathcal{H}}_{R,j} e^{-i\hat{L}_z \pi (k-1)/2} + V K_1^{\text{TM}}(T) \sin^2 \theta^{\text{TM}} - V \mathbf{M}^{\text{TM}}(T) \cdot \mathbf{B}. \quad (\text{D1})$$

In particular, by applying rotational operations to the CF Hamiltonian, the CF parameters at the  $k$ th  $R$  sites can be obtained in the following form:

$$e^{i\hat{L}_z \pi (k-1)/2} \hat{\mathcal{H}}_{\text{CF}} e^{-i\hat{L}_z \pi (k-1)/2} = \sum_{l,m} \frac{A_{l,k}^m \langle r^l \rangle}{a_{l,m}} \Theta_l^l t_l^m(\hat{\mathbf{L}}_k) \quad (\text{D2})$$

with

$$A_{l,k}^0 \langle r^l \rangle = A_l^0 \langle r^l \rangle \quad (\text{D3})$$

$$A_{l,k}^{-|m|} \langle r^l \rangle = \cos \left[ \frac{\pi}{2} |m|(k-1) \right] A_l^{-|m|} \langle r^l \rangle - \sin \left[ \frac{\pi}{2} |m|(k-1) \right] A_l^{|m|} \langle r^l \rangle \quad (\text{D4})$$

$$A_{l,k}^{|m|} \langle r^l \rangle = \sin \left[ \frac{\pi}{2} |m|(k-1) \right] A_l^{-|m|} \langle r^l \rangle + \cos \left[ \frac{\pi}{2} |m|(k-1) \right] A_l^{|m|} \langle r^l \rangle. \quad (\text{D5})$$

In the case of the analytical calculations using linear theory, the total MA energy can be written as a linear combination of  $A_{l,k}^m$ , and the expected value of the spherical tensor operator  $\langle C_0^{(l)}(\hat{\mathbf{L}}_k) \rangle$  is common for each  $k$ th  $R$  ion. Thus, all the terms including  $A_{l,k}^m$ , shown in Table VI, cancel and do not contribute to the macroscopic MA. Conversely, each  $R$  exhibits a noncollinear structure independently relative to the partial magnetization  $\mathbf{M}^{\text{TM}}(T)$  in the numerical diagonalization and

statistical calculations. Therefore, the complete cancellation of the  $A_{l,k}^m$  term in Table VI, which can be seen in the analytical formula, does not occur.

For  $\text{SmFe}_{11}\text{Ti}$  with the  $8i$  substitution, which is the most affected by the Ti substitution, the MA energy calculated using the numerical diagonalization and analytical formulas are represented by solid and dashed curves in Fig. 16, respectively. Due to the large value of  $A_{2,1(2)}^2 \langle r^2 \rangle = -320.8$  (320.8) K,  $\text{Sm}_{1(2)}$  exhibits a strong in-plane anisotropy proportional to the form  $A_{2,1(2)}^2 \cos 2\phi^{\text{TM}}$ . Therefore, these contributions completely cancel each other out. The result of numerical diagonalization also cancels the contribution to the same extent as in the analytical calculations. As a result, we can confirm that the MA energy of the bulk is well approximated by the analytical calculation method, where a collinear structure between the partial magnetization and the magnetic moment of each Sm ion is assumed.

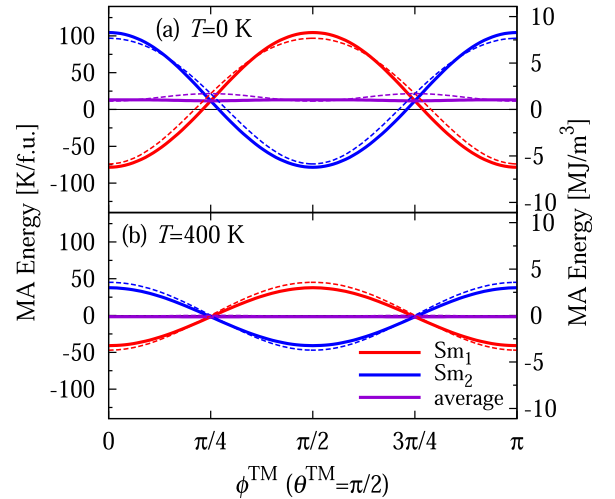


FIG. 16. Angular dependence of MA energy at (a)  $T = 0$  K and (b)  $T = 400$  K for two inequivalent sites and their averaged value ( $\text{Sm}_{1,2}$  and average) in  $\text{SmFe}_{11}\text{Ti}$  with  $8i$  substitution.  $\theta^{\text{TM}}$  and  $\phi^{\text{TM}}$  are the polar and azimuthal angle of partial magnetization  $\mathbf{M}^{\text{TM}}$ . The origin of the energy is taken at  $\theta^{\text{TM}} = 0$ . These results are obtained by applying Eq. (14) at  $\mathbf{B} = 0$  of Ref. [24].

- [1] T. Miyake, K. Terakura, Y. Harashima, H. Kino, and S. Ishibashi, *J. Phys. Soc. Jpn.* **83**, 043702 (2014).
- [2] Y. Hirayama, Y. K. Takahashi, S. Hirose, and K. Hono, *Scr. Mater.* **95**, 70 (2015).
- [3] S. Hirose, M. Nishino, and S. Miyashita, *Adv. Nat. Sci.: Nanotechnol.* **8**, 013002 (2017).
- [4] J. M. D. Coey, *Engineering* **6**, 119 (2020).
- [5] G. C. Hadjipanayis, A. M. Gabay, A. M. Schönhöbel, A. Martin-Cid, J. M. Baradarian, and D. Niarchos, *Engineering* **6**, 141 (2020).
- [6] K. Ohashi, Y. Tawara, R. Osugi, and M. Shimao, *J. Appl. Phys.* **64**, 5714 (1988).
- [7] B. Hu, H. Li, J. P. Gavigan, and J. M. D. Coey, *J. Phys.: Condens. Matter* **1**, 755 (1989).
- [8] T. Kuno, S. Suzuki, K. Urushibara, K. Kobayashi, N. Sakuma, M. Yano, A. Kato, and A. Manabe, *AIP Adv.* **6**, 025221 (2016).
- [9] Y. Hirayama, Y. K. Takahashi, S. Hirose, and K. Hono, *Scr. Mater.* **138**, 62 (2017).
- [10] A. M. Schönhöbel, R. Madugundo, O. Yu. Vekilova, O. Eriksson, H. C. Herper, J. M. Barandiarán, and G. C. Hadjipanayis, *J. Alloys Compd.* **786**, 969 (2019).
- [11] D. Ogawa, X. D. Xu, Y. K. Takahashi, T. Ohkubo, S. Hirose, and K. Hono, *Scr. Mater.* **164**, 140 (2019).
- [12] L. V. B. Diop, M. D. Kuz'min, Y. Skourski, K. P. Skokov, I. A. Radulov, and O. Gutfleish, *Phys. Rev. B* **102**, 064423 (2020).
- [13] D. Ogawa, T. Yoshioka, X. D. Xu, Y. K. Takahashi, H. Tsuchiura, T. Ohkubo, S. Hirose, and K. Hono, *J. Magn. Magn. Mater.* **497**, 165965 (2020).
- [14] H. Sepehri-Amin, Y. Tamazawa, M. Kobayashi, G. Saito, Y. K. Takahashi, D. Ogawa, T. Ohkubo, S. Hirose, M. Doi, T. Shima, and K. Hono, *Acta Mater.* **194**, 337 (2020).
- [15] P. Tozman, Y. K. Takahashi, H. Sepehri-Amin, D. Ogawa, S. Hirose, and K. Hono, *Acta Mater.* **178**, 114 (2019).
- [16] X. Tang, J. Li, A. K. Srinithi, H. Sepehri-Amin, T. Ohkubo, and K. Hono, *Scripta Mater.* **200**, 113925 (2021).
- [17] A. Makurenkova, D. Ogawa, P. Tozman, S. Okamoto, S. Nikitin, S. Hirose, and K. Hono, *Y. K. Takahashi J. Alloys. Compd.* **861**, 158477 (2021).
- [18] Y. Harashima, K. Terakura, H. Kino, S. Ishibashi, and T. Miyake, *Phys. Rev. B* **92**, 184426 (2015).
- [19] M. D. Kuz'min, M. Richter, and K. H. J. Buschow, *Solid State Commun.* **113**, 47 (2000).
- [20] Y. Harashima, K. Terakura, H. Kino, S. Ishibashi, and T. Miyake, *JPS Conf. Proc.* **5**, 011021 (2015).
- [21] W. Körner, G. Krugel, and C. Elsässer, *Sci. Rep.* **6**, 24686 (2016).
- [22] L. Ke and D. D. Johnson, *Phys. Rev. B* **94**, 024423 (2016).
- [23] P. Delange, S. Biermann, T. Miyake, and L. Pourovskii, *Phys. Rev. B* **96**, 155132 (2017).
- [24] T. Yoshioka, H. Tsuchiura, and P. Novák, *Phys. Rev. B* **102**, 184410 (2020).
- [25] H. Tsuchiura, T. Yoshioka, and P. Novák, *IEEE Trans. Magn.* **50**, 2105004 (2014).
- [26] T. Yoshioka and H. Tsuchiura, *Appl. Phys. Lett.* **112**, 162405 (2018).
- [27] H. Tsuchiura, T. Yoshioka, and P. Novák, *Scripata Mater.* **154**, 248 (2018).
- [28] S. Yamashita, D. Suzuki, T. Yoshioka, H. Tsuchiura, and P. Novák, *Phys. Rev. B* **102**, 214439 (2020).
- [29] S. A. Nikitin, I. S. Tereshina, V. N. Verbetskii, and A. A. Salamova, *Phys. Solid State* **40**, 258 (1998).
- [30] M. Yamada, H. Kato, H. Yamamoto, and Y. Nakagawa, *Phys. Rev. B* **38**, 620 (1988).
- [31] K. Hummler and M. Fähnle, *Phys. Rev. B* **53**, 3272 (1996).
- [32] S. G. Sankar, V. U. S. Rao, E. Segal, W. E. Wallace, W. G. D. Frederick, and H. J. Garrett, *Phys. Rev. B* **11**, 435 (1975).
- [33] H. W. de Wijn and A. M. van Diepen, and K. H. J. Buschow, *Phys. Stat. Sol. (b)* **76**, 11 (1976).
- [34] K. Stevens, *Proc. Phys. Soc.* **A65**, 209 (1952).
- [35] M. T. Hutchings, *Solid State Phys.* **16**, 227 (1964).
- [36] M. Fähnle, *J. Magn. Magn. Mater.* **151**, L5 (1995).
- [37] J. H. Van Vleck, *The Theory of Electric and Magnetic Susceptibilities* (Oxford University Press, Oxford, 1932).
- [38] M. D. Kuz'min, *J. Appl. Phys.* **92**, 6693 (2002).
- [39] N. Magnani, S. Carretta, E. Livioti, and G. Amoretti, *Phys. Rev. B* **67**, 144411 (2003).
- [40] Y. Harashima, K. Terakura, H. Kino, S. Ishibashi, and T. Miyake, *J. Appl. Phys.* **120**, 203904 (2016).
- [41] P. Blaha, K. Schwarz, G. Madsen, D. Kvasnicka, and J. Luitz, *WIEN2K, An Augmented Plane Wave + Local Orbitals Program for Calculating Crystal Properties* (Karlheinz Schwarz, TU Wien, Austria, 2001).
- [42] M. Richter, *J. Phys. D* **31**, 1017 (1998).
- [43] P. Novák, *Phys. Stat. Sol. B* **198**, 729 (1996).
- [44] M. Richter, P. M. Oppeneer, H. Eschrig, and B. Johansson, *Phys. Rev. B* **46**, 13919 (1992).
- [45] K. Hummler, T. Beuerle, and M. Fähnle, *J. Magn. Magn. Mater.* **115**, 207 (1992).
- [46] M. Diviš, K. Schwarz, P. Blaha, G. Hilscher, H. Michor, and S. Khmelevskiy, *Phys. Rev. B* **62**, 6774 (2000).
- [47] M. Diviš, J. Ruzs, H. Michor, G. Hilscher, P. Blaha, and K. Schwarz, *J. Alloys Compd.* **403**, 29 (2005).
- [48] P. Hohenberg and W. Kohn, *Phys. Rev.* **136**, B864 (1964).
- [49] W. Kohn and L. J. Sham, *Phys. Rev.* **140**, A1133 (1965).
- [50] M. Brooks, L. Nordström, and B. Johansson, *J. Phys. Condens. Mater* **3**, 3393 (1991).
- [51] M. Liebs, K. Hummler, and M. Fähnle, *Phys. Rev. B* **46**, 11201 (1992).
- [52] M. Liebs and M. Fähnle, *J. Magn. Magn. Mater.* **128**, L8 (1993).
- [53] M. D. Kuz'min, *Phys. Rev. Lett.* **94**, 107204 (2005).
- [54] D. Miura and A. Sakuma, *AIP Adv.* **8**, 075114 (2018).
- [55] K. Hummler and M. Fähnle, *Phys. Rev. B* **53**, 3290 (1996).
- [56] R. J. Elliott, *Magnetic Properties of Rare Earth Metals* (Plenum, New York, 1972), Chap. 1.
- [57] A. R. Edmonds, *Angular Momentum in Quantum Mechanics* (Princeton University Press, Princeton, 1960).
- [58] M. D. Kuz'min, *Phys. Rev. B* **46**, 8219 (1992).